



1 **10-year satellite-constrained fluxes of ammonia improve**  
2 **performance of chemistry transport models**

3  
4 **Nikolaos Evangeliou<sup>1,\*</sup>, Yves Balkanski<sup>2</sup>, Sabine Eckhardt<sup>1</sup>, Anne Cozic<sup>2</sup>, Martin**  
5 **Van Damme<sup>3</sup>, Pierre-François Coheur<sup>3</sup>, Lieven Clarisse<sup>3</sup>, Mark W. Shephard<sup>4</sup>,**  
6 **Karen E. Cady-Pereira<sup>5</sup>, Didier Hauglustaine<sup>2</sup>**

7  
8 <sup>1</sup>Norwegian Institute for Air Research (NILU), Department of Atmospheric and Climate  
9 Research (ATMOS), Kjeller, Norway.

10 <sup>2</sup>Laboratoire des Sciences du Climat et de l'Environnement (LSCE), CEA-CNRS-UVSQ,  
11 91191, Gif-sur-Yvette, France.

12 <sup>3</sup>Université libre de Bruxelles (ULB), Spectroscopy, Quantum Chemistry and Atmospheric  
13 Remote Sensing (SQUARES), Brussels, Belgium.

14 <sup>4</sup>Environment and Climate Change Canada, Toronto, Ontario M3H 5T4, Canada.

15 <sup>5</sup>Atmospheric and Environmental Research, Inc., Lexington, MA, USA.

16

17 \* Corresponding author: N. Evangeliou ([Nikolaos.Evangeliou@nilu.no](mailto:Nikolaos.Evangeliou@nilu.no))

18



19 **Abstract**

20 In recent years, ammonia emissions have been continuously increasing being almost four  
21 times higher than in the 20<sup>th</sup> century. Although an important species as its use as a fertilized  
22 sustains human living, ammonia has major consequences both for humans and the environment,  
23 because of its reactive gas phase chemistry that makes it easily convertible to particles. Despite  
24 its pronounced importance, yet, ammonia emissions are highly uncertain in most emission  
25 inventories. However, the great development of satellite remote sensing nowadays provides the  
26 opportunity for more targeting research in constraining ammonia emissions. Here, we used  
27 satellite measurements to calculate global ammonia emissions over the period 2008–2017.  
28 Then, the calculated ammonia emissions were fed to a chemistry transport model and ammonia  
29 concentrations were simulated for the period 2008–2017.

30 The simulated concentrations of ammonia were compared with ground measurements  
31 from Europe, North America and Southeastern Asia, as well as with satellite measurements.  
32 The satellite-constrained ammonia emissions represent global concentrations more accurately  
33 than state-of-the-art emissions, which underestimate ammonia with a factor of two. Calculated  
34 fluxes in the North China Plain were increased after 2015, not due to emission changes, but due  
35 to changes in sulfate emissions that resulted in less ammonia neutralization and hence in larger  
36 atmospheric loads. Emissions over Europe were also twice as much as those in traditional  
37 datasets with dominant sources to be industrial and agricultural applications. Four hot-spot  
38 regions of high ammonia emissions were seen in North America characterized by large  
39 agricultural activity (Colorado), animal breeding (Iowa, northern Texas and Kansas), animal  
40 farms (Salt Lake, Cache, and Utah) and animal breeding and agricultural practices (California).  
41 South America is dominated by ammonia emissions from biomass burning, which cause a  
42 strong seasonality. In Southeastern Asia, ammonia emissions from fertilizer plants in China,  
43 Pakistan, India and Indonesia are the most important, while a strong seasonality was observed  
44 with a spring and late summer peak due to rice and wheat cultivation. Modelled concentrations  
45 from the satellite-constrained ammonia emissions are overestimated in Eastern Europe, where  
46 state-of-the-art emissions capture observations better. Measurements of ammonia  
47 concentrations in North America were better reproduced with satellite-constrained emissions,  
48 while all emissions generally underestimate station concentrations in Southeastern Asia. The  
49 calculated ammonia emissions also reproduce global CrIS (Cross-track Infrared Sounder)  
50 observations more effectively.

51



## 52 **1 Introduction**

53 Ammonia ( $\text{NH}_3$ ) has received a lot of attention nowadays due to its major implications  
54 for the population and the environment (Erisman, 2004; Erisman et al., 2007). These include  
55 eutrophication of semi-natural ecosystems and acidification of soils (Stevens et al., 2010),  
56 secondary formation of particulate matter in the atmosphere (Anderson et al., 2003), and  
57 alteration of the global greenhouse balance (De Vries et al., 2011). More specifically in the  
58 troposphere, ammonia reacts with the abundant sulfuric and nitric acids (Malm, 2004)  
59 contributing 30 % to 50 % of the total aerosol mass of PM<sub>2.5</sub> and PM<sub>10</sub> (Anderson et al., 2003).  
60 Ammonium aerosols are therefore a very important component in regional and global aerosols  
61 processes (Xu and Penner, 2012) also having significant implications for human health (Aneja  
62 et al., 2009). Ammonia alters human health indirectly mainly through formation of PM<sub>2.5</sub> (Gu  
63 et al., 2014) that penetrate the human respiratory systems and deposit in the lungs and alveolar  
64 regions (Pope III et al., 2002) causing premature mortality (Lelieveld et al., 2015). As regards  
65 to the climate impact, the same ammonium aerosol particles affect Earth's radiative balance,  
66 both directly by scattering incoming radiation (Henze et al., 2012) and indirectly as cloud  
67 condensation nuclei (Abbatt et al., 2006). They may also cause visibility problems and  
68 contribute to haze effect due to secondary PM formation.

69 Sources of ammonia include wild animals (Sutton et al., 2000), ammonia-containing  
70 watersheds (Sørensen et al., 2003), traffic (Kean et al., 2009), sewage systems (Reche et al.,  
71 2012), humans (Sutton et al., 2000), biomass burning (Sutton et al., 2008) and domestic coal  
72 combustion (Fowler et al., 2004), volcanic eruptions (Sutton et al., 2008) and agriculture  
73 (Erisman et al., 2007). The latter is responsible for the majority of ammonia global atmospheric  
74 emissions. Specifically, in the United States and Europe about 80% of all emissions is related  
75 to agriculture (Leip et al., 2015). Emissions have increased considerably since pre-industrial  
76 times and are unlikely to decrease due to the growing demand for food and feed (Aneja et al.,  
77 2008).

78 The growing attention in ammonia levels has enabled many monitoring actions in Europe  
79 (European Monitoring and Evaluation Programme, EMEP), in Southeastern Asia (East Asia  
80 acid deposition NETwork) and in the North America (Ammonia Monitoring Network in the  
81 US, AMoN-US; National Air Pollution Surveillance Program (NAPS) sites in Canada) to  
82 record surface concentrations of ammonia continuously. Recently, several satellite products  
83 have been also developed in an effort to identify global levels of ammonia considering that the



84 relatively sparse existing monitoring network has an insufficient coverage for this purpose.  
85 These are derived from satellite sounders as the Infrared Atmospheric Sounding Interferometer  
86 (IASI) (Van Damme et al., 2017), the Atmospheric Infrared Sounder (AIRS) (Warner et al.,  
87 2017), the Cross-track Infrared Sounder (CrIS) (Shephard and Cady-Pereira, 2015) the  
88 Tropospheric Emission Spectrometer (TES) (Shephard et al., 2015), and Greenhouse Gases  
89 Observing Satellite (Someya et al., 2020). Both IASI and CrIS ammonia products are being  
90 continuously compared and evaluated against other observations and products. For example,  
91 against column-integrated levels measured by Fourier transform infrared spectroscopy (FTIR)  
92 (Dammers et al., 2016, 2017), ground-based measurements (Van Damme et al., 2015; Kharol  
93 et al., 2018), bottom-up emissions (Van Damme et al., 2018; Dammers et al., 2019) and  
94 atmospheric chemistry transport models (CTMs) (Shephard et al., 2020; Whitburn et al.,  
95 2016a).

96 Despite its importance, ammonia is a poorly quantified trace gas, with uncertainties over  
97 50% on the global emission budget and even higher on temporal and local scales (Dentener and  
98 Crutzen, 1994; Faulkner and Shaw, 2008; Reis et al., 2009). In the present paper, we grid 10  
99 years (2008–2017) of satellite measurements of ammonia retrieved from IASI to calculate  
100 monthly surface emissions (hereafter named NE) (see section 2). The same is done using the  
101 gridded IASI ammonia column concentrations from Van Damme et al. (2018) (named as VD0.5  
102 and VDgrlf) (see section 2). The three different emission inventories together with a state-of-  
103 the-art one, which is more often used by models (named as EGG), are then imported in a CTM  
104 to simulate ammonia for the same 10-year period. Finally, an evaluation of simulated surface  
105 concentrations against ground-based measurements from different monitoring stations and  
106 satellite products allow to quantify the improvements in ammonia emissions.

## 107 **2 Methods**

### 108 **2.1 Satellite ammonia**

#### 109 **2.1.1 IASI ammonia**

110 The Infrared Atmospheric Sounding Interferometer (IASI) onboard the MetOp-A satellite  
111 measures Earth's infrared radiation twice a day in a spectral range of 645–2,760  $\text{cm}^{-1}$  with an  
112 elliptical footprint (at nadir circular with a diameter of 12 km) at nadir (Clerbaux et al., 2009).  
113 Due to the larger thermal conditions that lead to smaller uncertainties, only morning data were  
114 used in the present assessment (Clarisse et al., 2010). The 10-year dataset used here is ANNI-  
115 NH3-v2.1R-I product (Van Damme et al., 2017). The Artificial Neural Network for IASI



116 (ANNI) algorithm converts the hyperspectral range index to an column-integrated  $\text{NH}_3$  value  
117 (Whitburn et al., 2016a). The dataset also provides cloud coverage for each measurement  
118 (August et al., 2012). Only measurements with a cloud fraction below 10% were processed in  
119 consistency with Van Damme et al. (2018). Cloud coverage was not provided for all  
120 measurements until March 2010 resulting in smaller data availability before that date. Although  
121 the retrieval algorithm uses a fixed vertical profile, extended validation of the resulting dataset  
122 has verified small uncertainties (Van Damme et al., 2015, 2018; Dammers et al., 2016;  
123 Whitburn et al., 2016b). For instance, Van Damme et al. (2018) reported a difference of  
124  $2\% \pm 24\%$  (global average) in column-integrated ammonia using different vertical profiles in  
125 the retrieval algorithm.

### 126 **2.1.2 CrIS ammonia**

127 The Cross-Track Infrared Sounder (CrIS) was first launched on the NASA Suomi  
128 National Polar-orbiting Partnership (S-NPP) satellite on 28 October 2011 in a sun-synchronous  
129 low Earth orbit. The CrIS sensor provides soundings of the atmosphere with a spectral  
130 resolution of  $0.625 \text{ cm}^{-1}$  (Shephard et al., 2015). One of the main advantages of CrIS is its  
131 improved vertical sensitivity of ammonia closer to the surface due to the low spectral noise of  
132  $\sim 0.04\text{K}$  at  $280\text{K}$  in the  $\text{NH}_3$  spectral region (Zavyalov et al., 2013) and the early afternoon  
133 overpass that typically coincides with high thermal contrast, which is optimal for thermal  
134 infrared sensitivity. The CrIS Fast Physical Retrieval (CFPR) (Shephard and Cady-Pereira,  
135 2015) retrieves an ammonia profile (14 levels) using a physics-based optimal estimation  
136 retrieval, which also provides the vertical sensitivity (averaging kernels) and an estimate of the  
137 retrieval errors (error covariance matrices) for each measurement. As peak sensitivity is  
138 typically in the boundary layer between 900 and 700 hPa ( $\sim 1$  to 3 km) (Shephard et al., 2020),  
139 the surface and total column concentrations are both highly correlated with the retrieved levels  
140 in the boundary layer. Shephard et al. (2020) reports estimated total column random  
141 measurement errors of 10–15%, with estimated total random errors of  $\sim 30\%$ . The individual  
142 profile retrieval levels have estimated random measurement errors of  $\sim 10$  to 30 %, with  
143 estimated total random errors increasing to 60 to 100% due to the limited vertical resolution.  
144 These vertical sensitivity and error output parameters are also useful for using CrIS  
145 observations in applications (e.g. data fusion, data assimilation; model-based emission  
146 inversions (e.g., Cao et al., 2020; Li et al., 2019) as a satellite observational operator can be  
147 generated in a robust manner. The detection limit of CrIS measurements has been calculated  
148 down to 0.3–0.5 ppbv (Shephard et al., 2020). CrIS ammonia has been evaluated against other  
149 observations over North America with the Ammonia Monitoring Network (AMoN) (Kharol et



150 al., 2018) and against ground-based Fourier transform infrared (FTIR) spectroscopy  
151 observations (Dammers et al., 2017) showing small differences and high correlations.

## 152 2.2 Inverse Distance Weighting (IDW) interpolation

153 To process large amounts of measurements in a 2-dimensional grid of high resolution,  
154 oversampling methods (Streets et al., 2013) can be used (Van Damme et al., 2018). However,  
155 considering that the resolution of the CTM is  $2.5^{\circ} \times 1.3^{\circ}$  (see section 2.4), there is no need to  
156 process the measurements on such a high-resolution grid and therefore an interpolation method  
157 was used. The method has been extensively used after the Chernobyl accident in 1986 to  
158 process more than 500 thousand deposition measurements over Europe (De Cort et al., 1998;  
159 Evangeliou et al., 2016).

160 IASI ammonia was interpolated onto a grid of  $2.5^{\circ} \times 1.3^{\circ}$  using a modified Inverse  
161 Distance Weighting (IDW) algorithm described by (Renka, 1988). This method is preferred  
162 due to its ease of use and to its high quality of interpolation. The IDW interpolation is defined  
163 by:

$$164 \quad \hat{v}(x, y) = \frac{\sum_{i=1}^n w_i v_i}{\sum_{i=1}^n w_i} \quad \text{Eq. 1}$$

165 where  $\hat{v}(x, y)$  is the interpolated value at point  $(x, y)$ ,  $w_1, \dots, w_i$  are the relative weights and  
166  $v_1, \dots, v_n$  are the observation values. The weights are defined by the inverse distance functions:

$$167 \quad w_i = \left( \frac{r_w - d_i}{r_w d_i} \right)^2 \quad \text{Eq. 2}$$

$$168 \quad \text{for } (r_w - d_i) = \begin{cases} r_w - d_i & \text{if } d_k < r_w, \\ 0 & \text{if } d_k \geq r_w. \end{cases}$$

169 where  $r_w$  denotes the radius of influence of the point  $(x_i, y_i)$ ,  $d_i$  the Euclidean distance  
170 between point  $(x, y)$  and  $(x_i, y_i)$ , and  $d_k$  is the threshold distance. We used a threshold  
171 distance ( $d_k$ ) of 50 km, which is similar to the size of each grid cell; different  $d_k$  values were  
172 included in a sensitivity study (see section 4.3). The Euclidean distance is calculated using  
173 Vincenty's formulae (Vincenty, 1975).

## 174 2.3 Emission flux calculation of ammonia

175 The emission fluxes of ammonia were calculated using a 1-dimensional box model that  
176 assumes first-order loss terms for ammonia and has been already used previously (Van Damme  
177 et al., 2018; Whitburn et al., 2016b). It takes into account the gridded column concentrations of  
178 ammonia that were calculated with the IDW interpolation method and all the potential removal



179 processes of ammonia occurring in a hypothetical atmospheric box according to the following  
180 equation:

$$181 \quad E_{NH_3} = M_{NH_3} / \tau \quad \text{Eq. 3}$$

182 where  $M_{NH_3}$  is the mass of ammonia in each atmospheric box (grid-cell) in molecules  $\text{cm}^{-2}$  and  
183  $\tau$  is the lifetime of ammonia in the box (given in seconds).

184 Van Damme et al. (2018) assumed a constant lifetime for ammonia, admitting that this is  
185 a limiting factor of their study on the basis that chemical loss and deposition are highly variable  
186 processes that can change the lifetime drastically. To tackle the large variability of the lifetime  
187 of ammonia, we used gridded lifetime calculated from a CTM. This gives robustness in the  
188 calculated emissions fluxes considering that at regions where sulfuric and nitric acids are  
189 abundant, the chemical loss will be more intense and, thus, lifetime will be much shorter  
190 affecting emissions dramatically.

191 The lifetime ( $\tau$ ) of ammonia in each grid-box results from the three processes affecting  
192 ammonia concentrations: transport ( $t_{trans}$ ) in and out of the grid-cell, chemical loss ( $t_{chem}$ )  
193 and deposition ( $t_{depo}$ ):

$$194 \quad \frac{1}{\tau} = \frac{1}{t_{trans}} + \frac{1}{t_{chem}} + \frac{1}{t_{depo}} \quad \text{Eq. 4}$$

195 In a CTM, the lifetime can be easily calculated from the species mass balance equation (Croft  
196 et al., 2014):

$$197 \quad \frac{dC(t)}{dt} = S(t) - \frac{C(t)}{\tau(t)} \quad \text{Eq. 5}$$

198 where  $C(t)$  is the atmospheric burden of ammonia at time  $t$ ,  $S(t)$  is the time-dependent source  
199 emission fluxes and  $\tau(t)$  is the removal timescale. Assuming steady-state conditions and  
200 considering that emission fluxes of ammonia are continuous, there is a quasi-equilibrium  
201 between sources and removals of ammonia (Dentener and Crutzen, 1994), and the modeled  
202 lifetime of ammonia  $\tau_{mod}$  can be defined as:

$$203 \quad \tau_{mod} = C_{NH_3} / L_{NH_3}^{trans,chem,depo} \quad \text{Eq. 6}$$

204 where  $C_{NH_3}$  is the atmospheric burden of ammonia and  $L_{NH_3}^{trans,chem,depo}$  is the total loss due to  
205 any process affecting ammonia in the model (transport, chemical reactions, deposition).

206 We calculate ammonia emission fluxes using IASI satellite measurements that we  
207 interpolated (section 2.2) to the model resolution ( $2.5^\circ \times 1.3^\circ$ ) and applying a variable lifetime  
208 taken from a CTM (hereafter NE emissions). We also calculate ammonia emissions from the



209 oversampled IASI data of Van Damme et al. (2018), after bilinear re-gridding to the model  
210 resolution ( $2.5^{\circ} \times 1.3^{\circ}$ ), applying a constant lifetime for ammonia of 12 hours (hereafter VD0.5  
211 emissions) and a variable lifetime from a CTM (hereafter VDgrlf emissions).

#### 212 **2.4 LMDz-OR-INCA chemistry transport model**

213 The Eulerian global CTM LMDz-OR-INCA was used to calculate ammonia lifetime, as  
214 well as to simulate ammonia concentrations from the emission fluxes calculated from IASI  
215 satellite products. The model couples the LMDz (Laboratoire de Météorologie Dynamique)  
216 General Circulation Model (GCM) (Hourdin et al., 2006) with the INCA (INteraction with  
217 Chemistry and Aerosols) model (Folberth et al., 2006; Hauglustaine et al., 2004) and with the  
218 land surface dynamical vegetation model ORCHIDEE (ORganizing Carbon and Hydrology In  
219 Dynamic Ecosystems) (Krinner et al., 2005). In the present configuration, the model has a  
220 horizontal resolution of  $2.5^{\circ} \times 1.3^{\circ}$ , the vertical dimension is divided into 39 hybrid vertical  
221 levels extending to the stratosphere. Large-scale advection of tracers is calculated from a  
222 monotonic finite-volume second-order scheme (Hourdin and Armengaud, 1999), deep  
223 convection is parameterized according to the scheme of Emanuel, (1991), while turbulent  
224 mixing in the planetary boundary layer (PBL) is based on a local second-order closure  
225 formalism. More information and a detailed evaluation of the GCM can be found in Hourdin et  
226 al. (2006).

227 The model simulates atmospheric transport of natural and anthropogenic aerosols  
228 recording both the number and the mass of aerosols. The aerosol size distribution is represented  
229 using a modal approach that consists of the superposition of 5 log-normal modes that represent  
230 both the size spectrum and whether the aerosol is soluble or insoluble (Schulz, 2007). The  
231 aerosols are treated in three particle modes, sub-micronic (diameter  $< 1 \mu\text{m}$ ) corresponding to  
232 the accumulation mode, micronic (diameter  $1\text{--}10 \mu\text{m}$ ) corresponding to coarse particles, and  
233 super-micronic or super coarse particles (diameter  $> 10 \mu\text{m}$ ). LMDz-OR-INCA accounts for  
234 emissions, transport (resolved and sub-grid scale), and dry and wet (in-cloud/below-cloud  
235 scavenging) deposition of chemical species and aerosols interactively. LMDz-OR-INCA  
236 includes a full chemical scheme for the ammonia cycle and nitrate particle formation, as well  
237 as a state-of-the-art  $\text{CH}_4/\text{NO}_x/\text{CO}/\text{NMHC}/\text{O}_3$  tropospheric photochemistry. Further details  
238 about specific reactions, reaction rates and other information entering into the description of  
239 the ammonia cycle can be found in Hauglustaine et al. (2014).



240 The global transport of ammonia was simulated from 2007 to 2017 (2007 was the spin-  
241 up period) by nudging the winds of the 6-hourly ERA Interim Reanalysis data (Dee et al., 2011)  
242 with a relaxation time of 10 days (Hourdin et al., 2006). For the calculation of ammonia's  
243 lifetime, the model ran with traditional emissions for anthropogenic, biomass burning and  
244 oceanic emission sources using emissions from ECLIPSEv5-GFED4-GEIA (hereafter called  
245 EGG) (Bouwman et al., 1997; Giglio et al., 2013; Klimont et al., 2017) .

## 246 **3 Results**

247 In this section, the main results of the monthly emissions (NE) are presented for the 10-  
248 year period (2008–2017) of IASI observations. We first describe the simulated ammonia  
249 lifetimes (section 3.1). Then, we explain the main characteristics of the obtained emissions  
250 (section 3.2) and compare them with those calculated using the IASI gridded products from  
251 Van Damme et al. (2018) (VD0.5 and VDgrlf), as well as the ones from the state-of-the-art  
252 inventories of EGG and EDGARv4.3.1-GFED4 (Crippa et al., 2016; Giglio et al., 2013) that  
253 are often used in CTMs (section 3.3). We finally turn our focus to hot-spot regions and  
254 document their seasonal variation in emissions (section 3.4).

### 255 **3.1 Modelled lifetime of ammonia**

256 The lifetime of ammonia has been reported to range from a few hours to a few days  
257 (Behera et al., 2013; Pinder et al., 2008) so ammonia can only be transported over relatively  
258 short distances. This short spread of ammonia is also due to the fact that (a) the majority of its  
259 emissions are surface ones (major source is agricultural activity), and (b) its surface deposition  
260 velocities are high for most surfaces (Hov et al., 1994). The atmospheric lifetimes of ammonia  
261 were summarized in Van Damme et al. (2018). Specifically, Quinn et al. (1990) and more  
262 recently Norman and Leck (2005) reported lifetimes of a few hours in the West Pacific, South  
263 Atlantic and Indian Oceans, which is in agreement with Flechard and Fowler (1998), who  
264 reported a 2-hour lifetime in an area of Scotland where most sources are of agricultural origin.  
265 Similar to them, Dammers et al. (2019) recently reported a lifetime estimated from satellite  
266 measurements of  $2.35 \pm 1.16$  hours for large point sources based on satellite measurements. The  
267 majority of ammonia lifetimes reported regionally or globally fall within 10 and 24 hours  
268 independently of the different approaches (Hauglustaine et al., 2014; Hertel et al., 2012; Möller  
269 and Schieferdecker, 1985; Sutton et al., 1993; Whitburn et al., 2016b), while Dentener and  
270 Crutzen (1994) reported slightly higher lifetimes within a range between 0.9 and 2.1 days  
271 depending on ammonia emission fraction of natural origin. Monthly averaged atmospheric



272 ammonia lifetimes in the present study were derived using the version of the LMDz-OR-INCA  
273 that includes non-methane hydrocarbons (Hauglustaine et al., 2004).

274 Ammonia lifetime depends on numerous factors such as the presence of ammonia's  
275 reactants (sulfuric and nitric acid), meteorological parameters (atmospheric water vapour, and  
276 temperature, atmospheric mixing and advection) and ammonia emissions. In ammonia-poor  
277 conditions, all ammonia is rapidly removed by neutralising sulfuric acid with an intermediate  
278 production of bisulfate. If ammonia increases further (ammonia-rich conditions), then reaction  
279 with nitric acid occurs forming nitric ammonium. At this point, the ammonia/sulfuric acid/nitric  
280 acid equilibrium becomes very fragile. If sulfate concentrations decrease, then free ammonia is  
281 produced, which gradually reacts with nitric acid resulting in production of aerosol phase nitric  
282 ammonium. But if particles are aqueous, then sulfate ions in solution increase the equilibrium  
283 vapour pressure of ammonia with nitric acid reversing the reaction towards gaseous phase  
284 reactants. So, sulfate reductions are linked with non-linear increases of aerosol nitrates and  
285 decreases of aerosol ammonium and water (Seinfeld and Pandis, 2000).

286 The calculated ammonia lifetime is shown in **Figure 1a**. The average lifetime was  
287 calculated to be  $11.6 \pm 0.6$  hours, which is in the range of the previously reported values. Lower  
288 values ( $\sim 10$  hours) were observed in clean remote areas characterized by low ammonia  
289 emissions (e.g., Amazon forest, Sahara and Australia), while in the rest of the globe the lifetime  
290 was closer to the average value. The highest lifetimes ( $\sim 16$  hours) occur over Southern Brazil  
291 and Venezuela, which are both areas with relatively high ammonia emissions and low sulfuric  
292 and nitric acid concentrations (**Figure 1c**). These conditions are characterized by a low  
293 atmospheric sulfuric and nitric acids availability to remove ammonia rapidly, hence causing an  
294 increase in lifetime.

### 295 **3.2 Satellite-constrained emissions**

296 The average ammonia emissions calculated from the 10-year IASI observations are  
297 shown in **Figure 1b** (also in **Figure S 1a**), the reactants' atmospheric burden in **Figure 1c** and  
298 their seasonal variability in **Figure 1d**. The year-by-year total ammonia emissions are depicted  
299 in **Figure S 1** with a monthly temporal resolution. Emissions decline from  $242 \text{ Tg yr}^{-1}$  in 2008  
300 to  $212 \text{ Tg yr}^{-1}$  in 2011. In 2012 – 2014, emissions show little variation ( $194$ ,  $204$  and  $195 \text{ Tg}$   
301  $\text{yr}^{-1}$ , respectively), before they increase steeply to  $248 \text{ Tg yr}^{-1}$  in 2015. Finally, in 2016 and 2017  
302 they remain at the same high level ( $197$  and  $227 \text{ Tg yr}^{-1}$ , respectively).



303 The global average annual emission calculated from VD0.5 amounts to 189 Tg (9-year  
304 average), which is comparable to the average of the 10-year period that we have calculated in  
305 the present study (average±sd:  $213\pm 18.1$  Tg yr<sup>-1</sup>). The increase in the emissions we calculate  
306 during 2015 and 2017 stand out. The explanation for these increases could be twofold. If sulfur  
307 dioxide emissions decreased over time, less sulfates are available to neutralize ammonia, hence  
308 resulting in higher ammonia column concentrations seen by IASI that could be attributed to  
309 new emissions erroneously (see section 2.3). If sulfur dioxide and sulfates presented a constant  
310 year-by-year pattern or even increased, then the calculated ammonia emissions would be likely  
311 realistic.

312 To sort out between these two possibilities, we used sulfur dioxide measurements from  
313 NASA's Ozone Monitoring Instrument (OMI, Yang et al., 2007) instrument, whereas sulfate  
314 column concentrations were taken from the Modern-Era Retrospective Analysis for Research  
315 and Applications, Version 2 (MERRA2, Gelaro et al., 2017) reanalysis data from NASA's  
316 Global Modeling and Assimilation Office (GMAO). Figure S 2 shows timeseries of column  
317 concentrations of sulfur dioxide and sulfates from OMI and MERRA2 averaged globally, for  
318 continental regions (Europe, North America, South America, Africa), as well as for regions  
319 where ammonia emissions are particularly high (India and Southeastern Asia, North China  
320 Plain). Although column concentrations of both sulfur dioxide and sulfates present strong  
321 interannual variability, they do not show significant changes on an annual basis. This indicates  
322 that sulfate amounts that neutralize ammonia and form ammonium sulfate are rather constant  
323 from year to year and, thus it is likely that the higher ammonia concentrations retrieved from  
324 IASI after 2015 are the result of an emission increase.

325 Another region of interest is the North China Plain, as it has been identified as an  
326 ammonia hotspot mainly due to extensive agricultural activities (Clarisse et al., 2009; Pan et  
327 al., 2018). Liu et al. (2018) reported a sulfur dioxide reduction of about 60% over the recent  
328 few years in the North China Plain, sulfates decreased by 50%, while ammonia emissions  
329 declined by only 7% due to change in agricultural practices. The suggested decrease in  
330 ammonia reactants over the North China Plain is illustrated by the calculated sulfur dioxide  
331 column concentration anomaly from OMI (Figure 2) and by the sulfate concentration anomaly  
332 from MERRA-2 after 2015 (the highest calculated one) (Figure S 3). However, the IASI-  
333 constrained ammonia emissions calculated here show only a tiny increase of  $0.19\pm 0.04$  kt y<sup>-1</sup>  
334 after 2015 in the North China Plain and of  $10\pm 3.1$  Tg y<sup>-1</sup> globally with respect to the 10-year



335 average (Figure 2). This is due to the change of SO<sub>2</sub> and NO<sub>x</sub> emission regulations in China,  
336 which in turn led to reduced inorganic matter (sulfates, nitrates and ammonium) resulting in  
337 regional increases of gaseous ammonia (Lachatre et al., 2019).

### 338 3.3 Comparison with traditional emission datasets

339 In this section, we quantify the main differences of our IASI-constrained emission dataset  
340 with other state-of-the-art inventories used in global models and for different applications (air  
341 quality, climate change etc...). Aside from comparing our emissions with those calculated using  
342 Van Damme et al. (2018) data with a constant lifetime (hereafter called VD0.5), we extend our  
343 comparison to more traditional datasets such as those of ECLIPSEv5-GFED4-GEIA (EGG) for  
344 2008–2017, and EDGARv4.3.1-GFED4 (Crippa et al., 2016; Giglio et al., 2013) for 2008–2012  
345 period. Finally, the ammonia emissions presented in this study (NE emissions) are compared  
346 to emissions calculated from Van Damme et al. (2018) gridded IASI column data applying a  
347 variable (modelled) ammonia lifetime presented in Figure 1b (hereafter referred as VDgrlf).

348 The 10-year comparison of our calculated emissions with VD0.5 is shown in Figure 3.  
349 The 10-year average difference amounts to  $29 \pm 15$  Tg yr<sup>-1</sup> (average  $\pm$ sd). In all years, the largest  
350 differences could be seen over Latin America and over tropical Africa. Our emissions (NE)  
351 were lower in the Indo-Gangetic Plain, and situated slightly more northerly. Northern India has  
352 been previously identified as a hot-spot region for ammonia, mainly due the importance of  
353 agricultural activities in the region (Kuttippurath et al., 2020; Tanvir et al., 2019).

354 Figure S 4 and Figure S 5 present a comparison of our calculated emissions with the basic  
355 state-of-the-art datasets of EGG and EDGARv4.3.1-GFED4, respectively. In both datasets,  
356 ammonia emissions remain almost constant over time (average  $\pm$ sd:  $65 \pm 2.8$  Tg yr<sup>-1</sup> and  $103 \pm 5.5$   
357 Tg yr<sup>-1</sup>, respectively). The total calculated ammonia emissions are up to three times lower than  
358 those calculated from NE (average  $\pm$ sd:  $213 \pm 18.1$  Tg yr<sup>-1</sup>) or from VD0.5 (9-year average:  $189$   
359 Tg yr<sup>-1</sup>). This results in 10-year annual differences that are very significant (average  $\pm$ sd:  
360  $150 \pm 19.3$  Tg yr<sup>-1</sup> and  $111 \pm 19.2$  Tg yr<sup>-1</sup>, respectively); the largest differences appear over South  
361 America, while European emissions are practically identical in all datasets. Emissions from  
362 South China Plain are much higher in the two traditional datasets than those calculated here.  
363 Based upon IASI retrievals, Liu et al. (2019) showed an increase of surface NH<sub>3</sub> concentrations  
364 trend of more than  $0.2 \mu\text{g N m}^{-3} \text{ yr}^{-1}$  in eastern China and of around  $0.1\text{--}0.2 \mu\text{g N m}^{-3} \text{ yr}^{-1}$  in  
365 northern Xinjiang during 2008–2016. Ammonia emissions derived over China in this work are



366 among the highest worldwide (**Figure S 1**), which agrees well with the 9-year average emissions  
367 calculated in VD0.5 inventory over China (see **Figure 3**). To assess to which extent emissions  
368 from EGG and EDGARv4.3.1-GFED4 are underestimated can only be done by comparing  
369 ammonia with ground or satellite observations.

370 The comparison of the annual ammonia emissions to the modified VDgrlf emissions is  
371 shown in **Figure S 6**. The latter showed a better agreement to the emissions presented in this  
372 study with mean annual different of  $14 \pm 19 \text{ Tg yr}^{-1}$  (average  $\pm$  sd). Previously observed emission  
373 differences in the two state-of-the-art inventories over South America and Africa have been  
374 now minimized, as well as the displacement north of the Indo-Gangetic Plain emissions remains  
375 important. Nevertheless, the smaller differences of our emissions from those of VDgrlf as  
376 compared with the respective difference from the VD0.5 emissions, show the large impact that  
377 a more realistic variable lifetime might have in emission calculations with this methodology.

### 378 **3.4 Site-specific ammonia emissions and seasonal variation**

379 **Figure 4** illustrates specific regions that show the largest ammonia emissions (Europe,  
380 North America, South America and Southeastern Asia). These emissions correspond to the  
381 IASI-constrained emissions calculated in this study (NE) and are presented as total annual  
382 emissions averaged over the 10-year period of study. At the bottom panels of the same figure,  
383 the seasonal variation of the emissions is shown for each of the four hot-spot regions and each  
384 of the 10 years of the study.

385 European total ammonia emissions were estimated to be  $15 \pm 2.2 \text{ Tg yr}^{-1}$  (average  $\pm$  sd),  
386 more than double compared with those reported in EGG ( $6.9 \pm 1.1 \text{ Tg yr}^{-1}$ ) and similar to those  
387 in VD0.5 ( $11 \text{ Tg yr}^{-1}$ ) or those in VDgrlf ( $11 \pm 1.0 \text{ Tg yr}^{-1}$ ). The greatest emissions were  
388 calculated for Belgium, the Netherlands and the Po Valley in Italy (**Figure 4**). High emissions  
389 are also found in North and Northwestern Germany and over Denmark. In contrast, very low  
390 emissions are found in Norway, Sweden and parts of the Alps. It is not possible to quantitatively  
391 distinguish between different sources of ammonia. It has been reported that approximately 75%  
392 of ammonia emissions in Europe originate from livestock production (Webb et al., 2005), and  
393 90% from agriculture in general (Leip et al., 2015). More specifically, ammonia is emitted from  
394 all stages of manure management, from livestock buildings during manure storage and  
395 application to land, as well as from livestock urine. These emissions are strong over most of  
396 Northwestern European countries, although sources like fertilization and non-agricultural



397 activities (traffic and urban emissions) can be also important. An example is Tange in Germany,  
398 which shows a late summer peak due to growing crops application. No obvious seasonality in  
399 the emissions can be seen for Europe as a whole, as the hot-spot regions are rather few compared  
400 to the overall surface of Europe. An exception to this stable emission situation over the year  
401 occurs during 2010 and during 2015, years for which a late summer peak. In 2010, large  
402 wildfires in Russia resulted in high ammonia emissions (R'Honi et al., 2013), while year 2015  
403 has been also characterized as an intense fire year (though not like 2010), with fires occurring  
404 in Eurasia (Min Hao et al., 2016).

405 North America and in particular the US (**Figure 4**) has been characterized by four hot-  
406 spot regions. First, a small region in Colorado, Central US, which is the location of a large  
407 agricultural region that traditionally releases large ammonia emissions (Malm et al., 2013).  
408 Another example is the state of Iowa (home to more than 20 million swine, 54 million chickens,  
409 and 4 million cattle), northern Texas and Kansas (beef cattle), and southern Idaho (dairy cattle)  
410 (McQuilling, 2016). Furthermore, the three major valleys in Salt Lake, in Cache, and in Utah  
411 in the midwestern US show an evident, but lower intensity hot-spot, as they are occupied by  
412 massive pig farms associated to open waste pits. The largest emissions were calculated for the  
413 San Joaquin Valley in California (vegetables, dairy, beef cattle and chickens) and further to the  
414 South (Tulare and Bakersfield), an area characterized by feedlots (Van Damme et al., 2018;  
415 McQuilling, 2016). North American annual ammonia emissions over the 10-year period were  
416 averaged  $1.1 \pm 0.1 \text{ Tg yr}^{-1}$  (average  $\pm$ sd). These values are over two orders of magnitude higher  
417 than those in EGG ( $0.062 \pm 0.0013 \text{ Tg yr}^{-1}$ ). Note that his estimate is three times lower than those  
418 reported in VD0.5 ( $3.1 \text{ Tg yr}^{-1}$ ) or in VDgrlf ( $3.4 \pm 0.5 \text{ Tg yr}^{-1}$ ). The 2008–2017 interannual  
419 variability (**Figure 4**) all show a minimum in winter. Maximum emissions were observed in late  
420 spring, due to the contribution from mineral fertilizer and manure application, in summer, due  
421 to influence of livestock housing emissions, and some years both in spring and summer (Makar  
422 et al., 2009; Zhu et al., 2013, 2015). A topographical dependence was also seen in midwest  
423 emissions that peaked in April, whereas over the rest of the US maximum emissions were  
424 appeared in summer (Paulot et al., 2014).

425 Ammonia emissions have different characteristics in South America and in Western  
426 Africa as both are fire-dominated regions. For simplicity we only present South America in  
427 **Figure 4**. This region is dominated by natural ammonia emissions mainly from forest, savanna  
428 and agricultural fires (Whitburn et al., 2014, 2016b) and volcanoes (Kajino et al., 2004;



429 Uematsu et al., 2004). This causes a strong seasonal variability in the ammonia emissions with  
430 the largest fluxes observed from August to October in all years (Figure 4). This strong  
431 dependence of South America from biomass burning emissions was first highlighted by Chen  
432 et al. (2013) and by van Marle et al. (2017). It also became particularly pronounced during the  
433 large wildfires in the Amazon rainforest in summer 2019 (Escobar, 2019). We estimated the  
434 10-year average ammonia emissions to be  $28 \pm 3.0 \text{ Tg yr}^{-1}$  (average  $\pm$  sd) in agreement with  
435 VD0.5 ( $22 \text{ Tg yr}^{-1}$ ) and VDgrlf ( $24 \pm 1.3 \text{ Tg yr}^{-1}$ ). The respective emissions in EGG are four  
436 times lower than these estimates ( $7.1 \pm 0.3 \text{ Tg yr}^{-1}$ ).

437 The last column to the right of Figure 4 presents the 10-year average annual ammonia  
438 emissions and their respective interannual variability in Southeastern Asia. We define this  
439 region spanning from  $70^\circ\text{E}$ – $130^\circ\text{E}$  in longitude and from  $0^\circ\text{N}$ – $45^\circ\text{N}$  in latitude. Ammonia  
440 emissions were estimated to be  $38 \pm 2.8 \text{ Tg yr}^{-1}$  (average  $\pm$  sd) similar to VD0.5 ( $36 \text{ Tg yr}^{-1}$ ) and  
441 VDgrlf ( $39 \pm 1.8 \text{ Tg yr}^{-1}$ ) and slightly higher than those presented in EGG ( $25 \pm 1.2 \text{ Tg yr}^{-1}$ ). They  
442 comprise ammonia fertilizer plants, such as in Pingsongxiang, Shizuishan, Zezhou-Gaoping,  
443 Chaerhan Salt Lake, Delingha, Midong-Fukang and Wucaiwan (China), Indo-Gangetic Plain  
444 (Pakistan and India), Gresik (Indonesia). China and India contribute more than half of total  
445 global ammonia emissions since the 1980s with the majority of these emissions to originate  
446 from rice cultivation followed by corn and wheat (crop-specific emissions). More specifically,  
447 emissions from these crops due to synthetic fertilizer and livestock manure applications are  
448 concentrated in North China Plain (Xu et al., 2018). Considering that Southeastern Asia is the  
449 largest agricultural contributor in the global ammonia budget, a strong seasonality in the  
450 emissions was observed. Temporal ammonia emissions peak in late summer of most years,  
451 when emissions from rice cultivation, synthetic fertilizer application and livestock manure  
452 spreading (Xu et al., 2016) are important, and in spring when wheat cultivation dominates  
453 (Datta et al., 2012). Of course, the respective emissions from biomass burning should also be  
454 mentioned. However, these are difficult to be distinguish and are expected to be a relatively  
455 small source compared to agricultural emissions.

## 456 4 Discussion

457 In this section, we conduct simulations over the 10-year period (2008–2017, 1-year spin-  
458 up), with all the emissions derived and compare the  $\text{NH}_3$  concentrations with ground based  
459 observations over Europe, North America, Southeastern Asia (section 4.1), and observations  
460 from CrIS (section 4.2). These simulations consist of: (i) a simulation using traditional



461 emissions from ECLIPSEv5 (Evaluating the CLimate and Air Quality ImPacts of Short-livEd  
462 Pollutants) for anthropogenic sources, GFED4 (Global Fire Emission Dataset) for biomass  
463 burning emissions and GEIA (Global Emissions InitiAtive) for oceanic sources from  
464 (Bouwman et al., 1997; Giglio et al., 2013; Klimont et al., 2017), where modelled lifetimes of  
465 ammonia were also calculated (EGG); (ii) a simulation using emissions calculated from IASI  
466 data from Van Damme et al. (2018) applying a constant lifetime of 12 hours for ammonia  
467 (VD0.5); (iii) a simulation using gridded emissions presented in the present paper (NE)  
468 calculated as described in section 2; and (iv) a simulation using emissions calculated from IASI  
469 data from Van Damme et al. (2018) applying a variable (modelled) lifetime (VDgrlf). Finally,  
470 we perform a sensitivity analysis in order to define the levels of uncertainty of our emissions in  
471 section 4.3 and discuss potential limitation of the present study in section 4.4.

#### 472 4.1 Validation against ground-based observations

473 **Figure 5** shows a comparison between modelled surface concentrations of ammonia with  
474 ground measurements from Europe (EMEP, <https://emep.int/mscw/>), North America (AMoN,  
475 <http://nadp.slh.wisc.edu/data/AMoN/>) and Southeastern Asia (EANET,  
476 <https://www.eanet.asia>). To avoid overplotting, the Gaussian kernel density estimation (KDE)  
477 was used, which is a non-parametric way to estimate the probability density function (PDF) of  
478 a random variable (Parzen, 1962):

$$479 \quad f(x) = \frac{1}{Nh} \sum_{i=1}^N K\left(\frac{x-x_i}{h}\right) \quad \text{Eq. 7}$$

480 where  $K$  is the kernel,  $x_i$  the univariate independent and identically distributed point of the  
481 relationship between modelled and measured ammonia and  $h$  is a smoothing parameter called  
482 the bandwidth. KDE is a fundamental data smoothing tool that attempts to infer characteristics  
483 of a population, based on a finite dataset. It weighs the distance of all points in each specific  
484 location along the distribution. If there are more points grouped locally, the estimation is higher  
485 as the probability of seeing a point at that location increases. The kernel function is the specific  
486 mechanism used to weigh the points across the data set and it uses the bandwidth to limit the  
487 scope of the function. The latter is computed using the Scott's factor (Scott, 2015). We also  
488 provide the mean fractional bias (MFB) for modelled and measured concentrations of ammonia  
489 as follows:

$$490 \quad MFB = \frac{1}{N} \frac{\sum_{i=1}^N (C_m - C_o)}{\sum_{i=1}^N \left(\frac{C_m + C_o}{2}\right)} \times 100\% \quad \text{Eq. 8}$$

491 where  $C_m$  and  $C_o$  are the modelled and measured ammonia concentrations and  $N$  is the total  
492 number of observations. MFB is a symmetric performance indicator that gives equal weights



493 to under- or over-estimated concentrations (minimum to maximum values range from -200%  
494 to 200%). Furthermore, we assess the deviation of the data from the line of best fit using the  
495 root mean square error (RMSE) defined as:

$$496 \quad RMSE = \sqrt{\sum_{i=1}^N \frac{(c_m - c_o)^2}{N}} \quad \text{Eq. 9}$$

497 From 134 European stations, nearly 300,000 measurements made at a daily to weekly  
498 temporal resolution over the period of study (2007–2018) are presented on **Figure 5**. All  
499 emission datasets underestimate ammonia surface concentration over Europe. The most  
500 accurate prediction of concentrations was achieved using the traditional EGG emissions that  
501 underestimated observations by 67%, also being the least scattered from the best fit  
502 ( $RMSE_{EGG} = 4.06 \mu\text{g N m}^{-3}$ ), followed by the emissions presented in this paper ( $MFB_{NE} =$   
503  $-72\%$ ,  $RMSE_{NE} = 4.65 \mu\text{g N m}^{-3}$ ), although they were more variable. VD0.5 or VDgrlf  
504 emissions further underestimated observations, though they were less sparse (**Figure 5d**). About  
505 12% of the modelled concentrations using EGG were outside of the 10-fold limit from the  
506 observations, in contrast to only 17% and 15% in VD0.5 and VDgrlf, and 20% in NE. With  
507 regards to the spatial comparison with the observed concentrations, all datasets cause  
508 overestimations in the ammonia concentrations predicted in Eastern Europe (station  
509 AM0001R). EGG appears to be the most accurate in Central Europe (all stations with suffix  
510 DE00), NE emissions in all Spanish stations (suffix ES00) and VD0.5 and VDgrlf emissions in  
511 Italian stations (**Figure S 7**).

512 The comparison of simulated ammonia concentrations to observations over North  
513 America includes 119 stations, which represent nearly 27,000 observations (Figure 6) with a  
514 weekly, bi-weekly or monthly resolution. The only emission dataset that lead to an  
515 underestimation of ammonia concentrations was EGG ( $MFB_{EGG} = -28\%$ ). Two others,  
516 VD0.5 and VDgrlf caused ammonia observations to be strongly overestimated ( $MFB_{VD0.5} =$   
517 **52% and  $MFB_{VDgrlf} = 54\%$** ), while NE slightly ( $MFB_{NE} = 32\%$ ). All inventories resulted  
518 in about the same variability in ammonia concentrations with RMSEs between 4.15 and 4.17  
519  $\mu\text{g N m}^{-3}$  (Figure 6). About 10% of the predicted concentrations using EGG emissions were at  
520 least 10 times off from the measured ones, more than twice the number of measurements  
521 compared to the other dataset. NE emissions better capture levels in the easternmost stations of  
522 the US (AL99, AR15, CT15, IL37, IN22, MI52, NY56, ON26) and in California (CA83) and  
523 Oklahoma (OK98), which are close to hot-spot regions (see section 3.4). EGG emissions  
524 perform better in Northwestern (ID03), Central (KS03) and several stations located over the



525 Eastern United States (KY03, KY98, OH09, AR03, IL46, KS03, GA41). The emission  
526 inventory VD0.5 leads to a very good agreement in ammonia concentrations over all stations  
527 of the North American continent (AL99, GA40, ID03, GA41, IL37, IL46, IN20, IN22, KS97,  
528 PA00, MD99, MI52, TN04, NM99, NY96, OH99, OK98) (Figure S 8).

529 In Southeastern Asia 62 stations from 13 countries were included in the comparison from  
530 the EANET monitoring network (Figure 7). These included about 8,000 surface measurements  
531 in monthly or 2-weekly resolution. All emission inventories underestimate station  
532 concentrations of EANET with MFBs between -102% (EGG) and -61% (VD0.5 and VDgrlf) ().  
533 The least spread model concentrations were those simulated using VD0.5 and VDgrlf  
534 ( $RMSE = 4.61 - 4.65 \mu g N m^{-3}$ ). Around 19% of model concentrations using EGG were  
535 outside the 10-fold limit of the  $1 \times 1$  line with observations, 12% using NE emissions and only  
536 5% and 6% using VD0.5 and VDgrlf, respectively. VD0.5 and VDgrlf emissions capture well  
537 the Japanese (suffix JPA) and Taiwanese stations (suffix THA). Given the short lifetime and  
538 the relatively coarse spatial scales, the model fails to capture the variability that exists within  
539 each gridbox (Figure S 9).

#### 540 4.2 Validation against satellite products

541 Here, we used surface ammonia concentrations from CrIS from 1st May 2012 to 31st  
542 December 2017 and we compared them with modelled ammonia concentrations using four  
543 emissions datasets (EGG, VD0.5, NE and VDgrlf), like in the previous section. The comparison  
544 is shown as PDF of surface modelled against CrIS concentrations of ammonia calculated with  
545 the Gaussian KDE in Figure 8. A total of 4.5 million surface measurements were used in the  
546 comparison with a global coverage. All datasets underestimated surface concentrations except  
547 NE emissions, which overestimate ammonia ( $MFB = +0.48$ ). The best fit was achieved for  
548 the VDgrlf emissions, which slightly underestimate ammonia ( $MFB = -0.37$ ), while 82% of  
549 the measurements were within one order of magnitude from the  $1 \times 1$  line, which is also shown  
550 by the small  $RMSE$ . VD0.5 emissions produced similar concentrations, with respect to the  
551  $RMSE$  and  $MFB$  values, whereas 79% of them were less than a 10-fold difference from the  
552 observations. NE emissions result in higher surface concentrations, also showing larger  
553  $RMSEs$ . However, 90% of the modelled concentrations were within a factor of 10 from the  
554 CrIS observation. In general, a better agreement for the most recent years 2015 – 2017 was  
555 achieved. The baseline EGG emissions resulted in significantly larger deviations of modelled



556 surface concentrations of ammonia from the CrIS observations, as shown in **Figure 8**  
557 comprising the largest *RMSE* and *MFB* values.

### 558 **4.3 Uncertainty analysis**

559 A sensitivity analysis in order to calculate the level of uncertainty that each of the  
560 parameter gives to the modelled surface concentrations of ammonia was also performed. The  
561 relative uncertainty was calculated as the standard deviation of ammonia's surface  
562 concentrations from a model ensemble of 10 members (**Table 1**) divided by the average. The  
563 first six members are the surface concentrations that resulted from simulations of ammonia  
564 emissions after perturbation of the Euclidian distance  $d_k$  in the parameters of the IDW  
565 interpolation. The remaining four members are simulated concentrations using the previously  
566 reported emissions datasets (EGG, VD0.5, NE and VDgrlf). The results are shown as a 10-year  
567 (2008–2017) annual average relative uncertainty in **Figure 9** and as annual average relative  
568 uncertainty of surface concentrations for every year of the 10-year period in **Figure S 10**.

569 The surface concentrations resulting from the different calculated emissions mainly  
570 affects oceanic regions, with values reaching 100%. The reason for this could be threefold.  
571 First, the IDW interpolation shows to be affected by severe outlier values, which are found in  
572 several oceanic regions (**Figure S 11**); this creates high gridded column ammonia  
573 concentrations and, in turn, fluxes at regions that are not supported by previous findings or  
574 measurements. Second, the methodology with which ammonia concentrations are retrieved in  
575 IASI has certain limitation, with respect to (i) the use of constant vertical profiles for ammonia,  
576 (ii) potential dependencies of total column ammonia and temperature that are not taken into  
577 account, and (iii) instrumental noise that can cause a high bias of the measurements (Whitburn  
578 et al., 2016a). Third, there is much less ammonia over the Ocean, hence the relative error bars  
579 are much larger. Large uncertainties in surface ammonia concentrations were observed in  
580 regions characterized by large anthropogenic contribution, such as North India, North China  
581 Plain and Central USA. Smaller uncertainties were found in Central Africa and in Amazonia,  
582 regions that are linked with episodic biomass burning emissions (**Figure 4**).

### 583 **4.4 Limitations of the present study**

584 We discuss the importance of certain limitations in the methodology of the present study  
585 and in the validation of the results. These limitations will also be commented upon in the overall  
586 conclusion of the paper.



587           Regarding the methodology, emissions of short-lived species are determined, among  
588 other methods, using top-down approaches. When only satellite measurements are available,  
589 they are usually averaged over a particular location and surface emissions are calculated using  
590 a mass balance approach (Lin et al., 2010; Zhao and Wang, 2009). This is done by assuming a  
591 1-dimensional box-model, where atmospheric transport between grids is assumed to be  
592 negligible and loss due to deposition or chemical reactions very fast. The solution to this  
593 problem is the use of Kernels (Boersma et al., 2008), which makes the computation of the  
594 emissions very intense. It has been reported that for resolutions, such as those used in the  
595 present paper ( $2.5^{\circ}\times 1.3^{\circ}$ ), non-local contributions to the ammonia emissions are relatively  
596 small (Turner et al., 2012). Although, the use of Kernels is the proper way to account for non-  
597 local contributions, we believe that negligible transport here is a fair assumption, due to the  
598 small lifetimes of ammonia calculated from the CTM ( $11.6\pm 0.6$  hours); therefore,  
599 transportation from the adjacent grid-cells should be small. Note that already this method has  
600 been suggested for short lived climate pollutants, it is not suitable for species with lifetime from  
601 days to weeks (e.g. black carbon, Bond et al., 2013).

602           Another limitation of the present study is that the same model is used for the calculation  
603 of the modelled lifetimes and for the validation of the emissions that were calculated using  
604 these lifetimes (NE and VDgrlf). A more accurate validation would require an independent  
605 model for the simulations of surface concentrations using these emissions.

## 606 **5 Conclusions**

607           In the present paper, satellite measurements from IASI were used to constrain global  
608 ammonia emissions over the period 2008–2017. The data were firstly processed to monthly  
609 ammonia column concentrations with a spatial resolution of  $2.5^{\circ}\times 1.3^{\circ}$ . Then, using gridded  
610 lifetime for ammonia calculated with a CTM, monthly fluxes were derived. This contrasts with  
611 previously reported methods that used a single constant lifetime. This enables a more accurate  
612 calculation in regions sensitive to the changing balance between nitrate and sulfate abundances.  
613 The calculated ammonia emission fluxes were then used to simulate ammonia concentrations  
614 for the period 2008–2017 (referred to as NE). The same simulations were repeated using  
615 baseline emissions from ECLIPSEv5-GFED4-GEIA (referred to as EGG), emissions  
616 constrained by Van Damme et al. (2018) IASI data using a constant lifetime for ammonia  
617 (named as VD0.5) and emissions based on Van Damme et al. (2018) retrievals using a modelled  
618 lifetime from a CTM (named as VDgrlf). The simulated surface concentrations of ammonia  
619 were compared with ground measurements over Europe (EMEP), North America (AMoN) and



620 Southeastern Asia (EANET), as well as with global satellite measurements from CrIS. The  
621 main conclusions can be summarized as follows:

- 622 • The 10-year average annual ammonia emissions calculated here (NE) were estimated to be  
623  $213 \pm 18.1 \text{ Tg yr}^{-1}$ , which is 15% higher than those in VD0.5 ( $189 \text{ Tg yr}^{-1}$ ), and 6% higher  
624 than those in VDgrlf ( $201 \pm 10.4 \text{ Tg yr}^{-1}$ ). These emission values amount to twice the  
625 published from datasets, such as EGG ( $65 \pm 2.8 \text{ Tg yr}^{-1}$ ) and EDGARv4.3.1-GFED4,  
626 ( $103 \pm 5.5 \text{ Tg yr}^{-1}$ ).
- 627 • In the North China Plain, a region characterized by intensive agricultural activities, a small  
628 increase of ammonia emissions is simulated after 2015. This is attributed to decreases in  
629 sulfur species, as revealed from OMI and MERRA-2 measurements. Less sulfates in the  
630 atmosphere leads to less ammonia neutralization and hence to larger loads in the  
631 atmospheric column as measured by IASI.
- 632 • In Europe, the 10-year average of ammonia emissions were estimated at  $15 \pm 2.2 \text{ Tg yr}^{-1}$   
633 (NE), twice as much as those in EGG ( $6.9 \pm 1.1 \text{ Tg yr}^{-1}$ ) and similar to those in VD0.5 ( $11$   
634  $\text{ Tg yr}^{-1}$ ) or VDgrlf ( $11 \pm 1.0 \text{ Tg yr}^{-1}$ ). The strongest emission fluxes were calculated over  
635 Belgium, Netherlands, Italy (Po Valley), Northwestern Germany and Denmark. These  
636 regions are known for industrial and agricultural applications, animal breeding activities,  
637 manure/slurry storage facilities and manure/slurry application to soils.
- 638 • Some hot-spot regions with high ammonia emissions were distinguished in North America:  
639 (i) in Colorado, due to large agricultural activity, (ii) in Iowa, northern Texas and Kansas,  
640 due to animal breeding, (iii) in Salt Lake, Cache, and Utah, due to animal farms associated  
641 with open waste pits and (iv) in California, due to animal breeding and agricultural  
642 practices. Ammonia emissions in North America were  $1.1 \pm 0.1 \text{ Tg yr}^{-1}$  or two orders of  
643 magnitude higher than in EGG ( $6.2 \pm 0.1 \text{ kt yr}^{-1}$ ) and three times lower than those in VD0.5  
644 ( $3.1 \text{ Tg yr}^{-1}$ ) or in VDgrlf ( $3.4 \pm 0.5 \text{ Tg yr}^{-1}$ ), with maxima observed in late spring, due to  
645 fertilization and manure application and summer, due to livestock emissions.
- 646 • South America is dominated by natural ammonia emissions mainly from forest, savanna  
647 and agricultural fires causing a strong seasonality with the largest fluxes between August  
648 and October. The 10-year average ammonia emissions were as high as  $28 \pm 3.0 \text{ Tg yr}^{-1}$   
649 similar to VD0.5 ( $22 \text{ Tg yr}^{-1}$ ) and VDgrlf ( $24 \pm 1.3 \text{ Tg yr}^{-1}$ ) and four times higher than EGG  
650 ( $7.1 \pm 0.3 \text{ Tg yr}^{-1}$ ).
- 651 • In Southeastern Asia, the 10-year average ammonia emissions were  $38 \pm 2.8 \text{ Tg yr}^{-1}$ , in  
652 agreement with VD0.5 ( $36 \text{ Tg yr}^{-1}$ ) and VDgrlf ( $39 \pm 1.8 \text{ Tg yr}^{-1}$ ) and slightly higher than



653 those in EGG ( $25 \pm 1.2 \text{ Tg yr}^{-1}$ ). The main sources were from fertilizer plants in China,  
654 Pakistan, India and Indonesia. China and India hold the largest share in the ammonia  
655 emissions mainly due to rice, corn and wheat cultivation. A strong seasonality in the  
656 emissions was observed with a late summer peak in most years, due to rice cultivation,  
657 synthetic fertilizer and livestock manure applications and in spring due to wheat  
658 cultivation.

659 • About 88% of the modelled concentrations over Europe using EGG were inside the 10-  
660 fold limit from the observations, higher than those with VD0.5 (83%), VDgrlf (85%) and  
661 NE (80%). All emission datasets overestimate of ammonia in Eastern Europe, EGG  
662 captures better Central Europe, NE emissions predict concentrations in Spain and VD0.5  
663 with VDgrlf emissions in Italy.

664 • In North America, 90% of the modelled concentrations using EGG emissions were less  
665 than 10 times different from the measured ones; more than 95% of the modelled  
666 concentrations in North American stations were in the same range using NE, VD0.5 and  
667 VDgrlf emissions. NE emissions better capture levels in the easternmost stations of the US  
668 closer to the respective hot-spot regions, whereas EGG emissions perform better in  
669 Northwestern and Central USA. VD0.5 and VDgrlf emissions perform well in most of the  
670 North American stations.

671 • All emissions underestimate station concentrations in Southeastern Asia. The least spread  
672 model concentrations were those simulated using VD0.5 and VDgrlf. About 81% of  
673 modelled concentrations using EGG were in the 10-fold limit of the  $1 \times 1$  line with  
674 observations, 88% using NE and only 95% and 94% using VD0.5 and VDgrlf, respectively.  
675 VD0.5 and VDgrlf emissions capture well the Japanese and Taiwanese stations.

676 • The comparison of the modelled ammonia with satellite observations from CrIS globally  
677 showed that the best agreement was achieved using the VDgrlf emissions in 2012–2014.  
678 After 2015, all satellite retrieved emissions show a better agreement with CrIS  
679 concentrations.

680 Overall, the satellite-constrained ammonia emissions calculated using a variable lifetime  
681 appear to give more realistic concentrations, with respect to station and satellite measurements.  
682 Accordingly, state-of-the-art emissions appear to underestimate ammonia significantly.

683



684 *Data availability.* All data and python scripts used for the present publication are open through  
685 the web address <https://folk.nilu.no/~nikolaos/AMMONIA/> or can be obtained from the  
686 corresponding author upon request.

687

688 *Competing interests.* The authors declare no competing interests.

689

690 *Acknowledgements.* This study was supported by the Research Council of Norway (project  
691 ID: 275407, COMBAT – Quantification of Global Ammonia Sources constrained by a  
692 Bayesian Inversion Technique). Lieven Clarisse and Martin Van Damme are respectively a  
693 research associate and a postdoctoral researcher supported by the F.R.S.–FNRS.

694

695 *Author contributions.* N.E. performed the simulations, analyses, wrote and coordinated the  
696 paper. S.E. contributed to the lifetime calculations. Y.B., D.H. and A.C. set up the CTM model.  
697 M.V.D., P.-F.C. and L.C. provided the IASI data, while M.W.S. and K.E.C.-P. provided the  
698 observations from CrIS. All authors contributed to the final version of the manuscript.

699

## 700 **References**

- 701 Abbatt, J. P. D., Benz, S., Cziczo, D. J., Kanji, Z., Lohmann, U. and Mohler, O.: Solid  
702 Ammonium Sulfate Aerosols as Ice Nuclei: A Pathway for Cirrus Cloud Formation,  
703 *Science* (80-. ), (September), 1770–1773, 2006.
- 704 Anderson, N., Strader, R. and Davidson, C.: Airborne reduced nitrogen: Ammonia  
705 emissions from agriculture and other sources, *Environ. Int.*, 29(2–3), 277–286,  
706 doi:10.1016/S0160-4120(02)00186-1, 2003.
- 707 Aneja, V. P., Schlesinger, W. H. and Erisman, J. W.: Farming pollution, *Nat. Geosci.*,  
708 1(7), 409–411 [online] Available from: <http://dx.doi.org/10.1038/ngeo236>, 2008.
- 709 Aneja, V. P., Schlesinger, W. H. and Erisman, J. W.: Effects of agriculture upon the  
710 air quality and climate: Research, policy, and regulations, *Environ. Sci. Technol.*,  
711 43(12), 4234–4240, doi:10.1021/es8024403, 2009.
- 712 August, T., Klaes, D., Schlüssel, P., Hultberg, T., Crapeau, M., Arriaga, A., O’Carroll,  
713 A., Coppens, D., Munro, R. and Calbet, X.: IASI on Metop-A: Operational Level 2  
714 retrievals after five years in orbit, *J. Quant. Spectrosc. Radiat. Transf.*, 113(11),  
715 1340–1371, doi:10.1016/j.jqsrt.2012.02.028, 2012.
- 716 Behera, S. N., Sharma, M., Aneja, V. P. and Balasubramanian, R.: Ammonia in the  
717 atmosphere: A review on emission sources, atmospheric chemistry and deposition  
718 on terrestrial bodies, *Environ. Sci. Pollut. Res.*, 20(11), 8092–8131,  
719 doi:10.1007/s11356-013-2051-9, 2013.
- 720 Boersma, K. F., Jacob, D. J., Bucsela, E. J., Perring, A. E., Dirksen, R., van der A, R.  
721 J., Yantosca, R. M., Park, R. J., Wenig, M. O., Bertram, T. H. and Cohen, R. C.:  
722 Validation of OMI tropospheric NO<sub>2</sub> observations during INTEX-B and application to  
723 constrain NO<sub>x</sub> emissions over the eastern United States and Mexico, *Atmos.*  
724 *Environ.*, 42(19), 4480–4497, doi:10.1016/j.atmosenv.2008.02.004, 2008.
- 725 Bond, T. C., Doherty, S. J., Fahey, D. W., Forster, P. M., Berntsen, T., Deangelo, B.  
726 J., Flanner, M. G., Ghan, S., Kärcher, B., Koch, D., Kinne, S., Kondo, Y., Quinn, P.



- 727 K., Sarofim, M. C., Schultz, M. G., Schulz, M., Venkataraman, C., Zhang, H., Zhang,  
728 S., Bellouin, N., Guttikunda, S. K., Hopke, P. K., Jacobson, M. Z., Kaiser, J. W.,  
729 Klimont, Z., Lohmann, U., Schwarz, J. P., Shindell, D., Storelvmo, T., Warren, S. G.  
730 and Zender, C. S.: Bounding the role of black carbon in the climate system: A  
731 scientific assessment, *J. Geophys. Res. Atmos.*, 118(11), 5380–5552,  
732 doi:10.1002/jgrd.50171, 2013.
- 733 Bouwman, A. F., Lee, D. S., Asman, W. A. H., Dentener, F. J., Van Der Hoek, K. W.  
734 and Olivier, J. G. J.: A global high-resolution emission inventory for ammonia, *Global*  
735 *Biogeochem. Cycles*, 11(4), 561–587, doi:10.1029/97GB02266, 1997.
- 736 Cao, H., Henze, D. K., Shephard, M. W., Dammers, E., Cady-Pereira, K., Alvarado,  
737 M., Lonsdale, C., Luo, G., Yu, F., Zhu, L., Danielson, C. G. and Edgerton, E. S.:  
738 Inverse modeling of NH<sub>3</sub> sources using CrIS remote sensing measurements,  
739 *Environ. Res. Lett.*, in press, doi:10.1088/1748-9326/abb5cc, 2020.
- 740 Chen, Y., Morton, D. C., Jin, Y., Gollatz, G. J., Kasibhatla, P. S., Van Der Werf, G.  
741 R., Defries, R. S. and Randerson, J. T.: Long-term trends and interannual variability  
742 of forest, savanna and agricultural fires in South America, *Carbon Manag.*, 4(6), 617–  
743 638, doi:10.4155/cmt.13.61, 2013.
- 744 Clarisse, L., Clerbaux, C., Dentener, F., Hurtmans, D. and Coheur, P.-F.: Global  
745 ammonia distribution derived from infrared satellite observations, *Nat. Geosci.*, 2(7),  
746 479–483 [online] Available from: <http://dx.doi.org/10.1038/ngeo551>, 2009.
- 747 Clarisse, L., Shephard, M. W., Dentener, F., Hurtmans, D., Cady-Pereira, K.,  
748 Karagulian, F., Van Damme, M., Clerbaux, C. and Coheur, P. F.: Satellite monitoring  
749 of ammonia: A case study of the San Joaquin Valley, *J. Geophys. Res.*, 115,  
750 doi:10.1029/2009jd013291, 2010.
- 751 Clerbaux, C., Boynard, A., Clarisse, L., George, M., Hadji-Lazaro, J., Herbin, H.,  
752 Hurtmans, D., Pommier, M., Razavi, A., Turquety, S., Wespes, C. and Coheur, P.-F.:  
753 Monitoring of atmospheric composition using the thermal infrared IASI/MetOp  
754 sounder, *Atmos. Chem. Phys.*, 9(16), 6041–6054, doi:10.5194/acp-9-6041-2009,  
755 2009.
- 756 De Cort, M., Dubois, G., Fridman, S. D., Germenchuk, M., G., Izrael, Y. A., Janssens,  
757 A., Jones, A. R., Kelly, G., N., Kvasnikova, E., V., Matveenko, I., I., Nazarov, I., N.,  
758 Pokumeiko, Y., M., Sitak, V. A., Stukin, E., D., Tabachny, L., Y., Tsaturov, Y. S. and  
759 Avdyushin, S., I.: Atlas of caesium deposition on Europe after the Chernobyl  
760 accident, EU - Office for Official Publications of the European Communities,  
761 Luxembourg., 1998.
- 762 Crippa, M., Janssens-Maenhout, G., Dentener, F., Guizzardi, D., Sindelarova, K.,  
763 Muntean, M., Van Dingenen, R. and Granier, C.: Forty years of improvements in  
764 European air quality: Regional policy-industry interactions with global impacts,  
765 *Atmos. Chem. Phys.*, 16(6), 3825–3841, doi:10.5194/acp-16-3825-2016, 2016.
- 766 Croft, B., Pierce, J. R. and Martin, R. V.: Interpreting aerosol lifetimes using the  
767 GEOS-Chem model and constraints from radionuclide measurements, *Atmos. Chem.*  
768 *Phys.*, 14(8), 4313–4325, doi:10.5194/acp-14-4313-2014, 2014.
- 769 Van Damme, M., Clarisse, L., Dammers, E., Liu, X., Nowak, J. B., Clerbaux, C.,  
770 Flechard, C. R., Galy-Lacaux, C., Xu, W., Neuman, J. A., Tang, Y. S., Sutton, M. A.,  
771 Erisman, J. W. and Coheur, P. F.: Towards validation of ammonia (NH<sub>3</sub>)  
772 measurements from the IASI satellite, *Atmos. Meas. Tech.*, 8(3), 1575–1591,  
773 doi:10.5194/amt-8-1575-2015, 2015.
- 774 Van Damme, M., Whitburn, S., Clarisse, L., Clerbaux, C., Hurtmans, D. and Coheur,  
775 P.: Version 2 of the IASI NH<sub>3</sub> neural network retrieval algorithm : near-real-time and  
776 reanalysed datasets, , 4905–4914, 2017.



- 777 Van Damme, M., Clarisse, L., Whitburn, S., Hadji-Lazaro, J., Hurtmans, D., Clerbaux,  
778 C. and Coheur, P.-F.: Industrial and agricultural ammonia point sources exposed,  
779 *Nature*, 564(7734), 99–103, doi:10.1038/s41586-018-0747-1, 2018.
- 780 Dammers, E., Palm, M., Van Damme, M., Vigouroux, C., Smale, D., Conway, S.,  
781 Toon, G. C., Jones, N., Nussbaumer, E., Warneke, T., Petri, C., Clarisse, L.,  
782 Clerbaux, C., Hermans, C., Lutsch, E., Strong, K., Hannigan, J. W., Nakajima, H.,  
783 Morino, I., Herrera, B., Stremme, W., Grutter, M., Schaap, M., Kruit, R. J. W., Notholt,  
784 J., Coheur, P. F. and Erisman, J. W.: An evaluation of IASI-NH 3 with ground-based  
785 Fourier transform infrared spectroscopy measurements, *Atmos. Chem. Phys.*,  
786 16(16), 10351–10368, doi:10.5194/acp-16-10351-2016, 2016.
- 787 Dammers, E., Shephard, M. W., Palm, M., Cady-pereira, K., Capps, S., Lutsch, E.,  
788 Strong, K., Hannigan, J. W., Ortega, I., Toon, G. C., Stremme, W. and Grutter, M.:  
789 Validation of the CrIS fast physical NH 3 retrieval with ground-based FTIR, , 87,  
790 2645–2667, 2017.
- 791 Dammers, E., McLinden, C. A., Griffin, D., Shephard, M. W., Van Der Graaf, S.,  
792 Lutsch, E., Schaap, M., Gainairu-Matz, Y., Fioletov, V., Van Damme, M., Whitburn,  
793 S., Clarisse, L., Cady-Pereira, K., Clerbaux, C., Francois Coheur, P. and Erisman, J.  
794 W.: NH<sub>3</sub> emissions from large point sources derived from CrIS and IASI satellite  
795 observations, *Atmos. Chem. Phys.*, 19(19), 12261–12293, doi:10.5194/acp-19-  
796 12261-2019, 2019.
- 797 Datta, A., Sharma, S. K., Harit, R. C., Kumar, V., Mandal, T. K. and Pathak, H.:  
798 Ammonia emission from subtropical crop land area in india, *Asia-Pacific J. Atmos.*  
799 *Sci.*, 48(3), 275–281, doi:10.1007/s13143-012-0027-1, 2012.
- 800 Dee, D. P., Uppala, S. M., Simmons, A. J., Berrisford, P., Poli, P., Kobayashi, S.,  
801 Andrae, U., Balmaseda, M. A., Balsamo, G., Bauer, P., Bechtold, P., Beljaars, A. C.  
802 M., van de Berg, L., Bidlot, J., Bormann, N., Delsol, C., Dragani, R., Fuentes, M.,  
803 Geer, A. J., Haimberger, L., Healy, S. B., Hersbach, H., H??lm, E. V., Isaksen, L.,  
804 K??llberg, P., K??hler, M., Matricardi, M., McNally, A. P., Monge-Sanz, B. M.,  
805 Morcrette, J. J., Park, B. K., Peubey, C., de Rosnay, P., Tavolato, C., Th??paut, J. N.  
806 and Vitart, F.: The ERA-Interim reanalysis: Configuration and performance of the  
807 data assimilation system, *Q. J. R. Meteorol. Soc.*, 137(656), 553–597,  
808 doi:10.1002/qj.828, 2011.
- 809 Dentener, F. J. and Crutzen, P. J.: A 3-Dimensional Model Of The Global Ammonia  
810 Cycle, *J. Atmos. Chem.*, 19(4), 331–369, doi:10.1007/bf00694492, 1994.
- 811 Emanuel, K. A.: A Scheme for Representing Cumulus Convection in Large-Scale  
812 Models, *J. Atmos. Sci.*, 48(21), 2313–2329, doi:10.1175/1520-  
813 0469(1991)048<2313:ASFRCC>2.0.CO;2, 1991.
- 814 Erisman, J. A. N. W.: The Nanjing Declaration on Management of Reactive Nitrogen,  
815 , 54(4), 286–287, 2004.
- 816 Erisman, J. W., Bleeker, A., Galloway, J. and Sutton, M. S.: Reduced nitrogen in  
817 ecology and the environment, *Environ. Pollut.*, 150(1), 140–149,  
818 doi:10.1016/j.envpol.2007.06.033, 2007.
- 819 Escobar, H.: Amazon fires clearly linked to deforestation, scientists say, *Science* (80-  
820 .), 365(6456), 853, doi:10.1126/science.365.6456.853, 2019.
- 821 Evangeliou, N., Hamburger, T., Talerko, N., Zibtsev, S., Bondar, Y., Stohl, A.,  
822 Balkanski, Y., Mousseau, T. A. and Møller, A. P.: Reconstructing the Chernobyl  
823 Nuclear Power Plant (CNPP) accident 30 years after. A unique database of air  
824 concentration and deposition measurements over Europe, *Environ. Pollut.*, (August),  
825 doi:10.1016/j.envpol.2016.05.030, 2016.
- 826 Faulkner, W. B. and Shaw, B. W.: Review of ammonia emission factors for United



- 827 States animal agriculture, *Atmos. Environ.*, 42(27), 6567–6574,  
828 doi:10.1016/j.atmosenv.2008.04.021, 2008.
- 829 Flechard, C. R. and Fowler, D.: Atmospheric ammonia at a moorland site. I: The  
830 meteorological control of ambient ammonia concentrations and the influence of local  
831 sources, *Q. J. R. Meteorol. Soc.*, 124(547), 733–757, doi:10.1256/smsqj.54704,  
832 1998.
- 833 Folberth, G. A., Hauglustaine, D. A., Lathièrre, J. and Brocheton, F.: Interactive  
834 chemistry in the Laboratoire de Météorologie Dynamique general circulation model:  
835 model description and impact analysis of biogenic hydrocarbons on tropospheric  
836 chemistry, *Atmos. Chem. Phys.*, 6(8), 2273–2319, doi:10.5194/acp-6-2273-2006,  
837 2006.
- 838 Fowler, D., Muller, J. B. A., Smith, R. I., Dragosits, U., Skiba, U., Sutton, M. A. and  
839 Brimblecombe, P.: A CHRONOLOGY OF NITROGEN DEPOSITION IN THE UK, , 2,  
840 9–23, 2004.
- 841 Gelaro, R., McCarty, W., Suárez, M. J., Todling, R., Molod, A., Takacs, L., Randles,  
842 C. A., Darmenov, A., Bosilovich, M. G., Reichle, R., Wargan, K., Coy, L., Cullather,  
843 R., Draper, C., Akella, S., Buchard, V., Conaty, A., da Silva, A. M., Gu, W., Kim, G.  
844 K., Koster, R., Lucchesi, R., Merkova, D., Nielsen, J. E., Partyka, G., Pawson, S.,  
845 Putman, W., Rienecker, M., Schubert, S. D., Sienkiewicz, M. and Zhao, B.: The  
846 modern-era retrospective analysis for research and applications, version 2 (MERRA-  
847 2), *J. Clim.*, 30(14), 5419–5454, doi:10.1175/JCLI-D-16-0758.1, 2017.
- 848 Giglio, L., Randerson, J. T. and van der Werf, G. R.: Analysis of daily, monthly, and  
849 annual burned area using the fourth-generation global fire emissions database  
850 (GFED4), *J. Geophys. Res. Biogeosciences*, 118, 317–328, doi:10.1002/jgrg.20042,  
851 2013, 2013.
- 852 Gu, B., Sutton, M. A., Chang, S. X., Ge, Y. and Chang, J.: Agricultural ammonia  
853 emissions contribute to China's urban air pollution, *Front. Ecol. Environ.*, 12(5), 265–  
854 266, doi:10.1890/14.WB.007, 2014.
- 855 Hauglustaine, D. A., Hourdin, F., Jourdain, L., Filiberti, M.-A., Walters, S., Lamarque,  
856 J.-F. and Holland, E. A.: Interactive chemistry in the Laboratoire de Meteorologie  
857 Dynamique general circulation model: Description and background tropospheric  
858 chemistry evaluation, *J. Geophys. Res.*, 109(D04314), doi:10.1029/2003JD003957,  
859 2004.
- 860 Hauglustaine, D. A., Balkanski, Y. and Schulz, M.: A global model simulation of  
861 present and future nitrate aerosols and their direct radiative forcing of climate, *Atmos.*  
862 *Chem. Phys.*, 14(20), 11031–11063, doi:10.5194/acp-14-11031-2014, 2014.
- 863 Henze, D. K., Shindell, D. T., Akhtar, F., Spurr, R. J. D., Pinder, R. W., Loughlin, D.,  
864 Kopacz, M., Singh, K. and Shim, C.: Spatially Refined Aerosol Direct Radiative  
865 Forcing Efficiencies, *Environ. Sci. Technol.*, 46, 9511–9518, doi:10.1021/es301993s,  
866 2012.
- 867 Hertel, O., Skjoth, C. A., Reis, S., Bleeker, A., Harrison, R. M., Cape, J. N., Fowler,  
868 D., Skiba, U., Simpson, D., Jickells, T., Kulmala, M., Gyldenkerne, S., Sorensen, L.  
869 L., Erisman, J. W. and Sutton, M. A.: Governing processes for reactive nitrogen  
870 compounds in the European atmosphere, *Biogeosciences*, 9(12), 4921–4954,  
871 doi:10.5194/bg-9-4921-2012, 2012.
- 872 Hourdin, F. and Armengaud, A.: The Use of Finite-Volume Methods for Atmospheric  
873 Advection of Trace Species. Part I: Test of Various Formulations in a General  
874 Circulation Model, *Mon. Weather Rev.*, 127(5), 822–837, doi:10.1175/1520-  
875 0493(1999)127<0822:TUOFVM>2.0.CO;2, 1999.
- 876 Hourdin, F., Musat, I., Bony, S., Braconnot, P., Codron, F., Dufresne, J. L., Fairhead,



- 877 L., Filiberti, M. A., Friedlingstein, P., Grandpeix, J. Y., Krinner, G., LeVan, P., Li, Z. X.  
878 and Lott, F.: The LMDZ4 general circulation model: Climate performance and  
879 sensitivity to parametrized physics with emphasis on tropical convection, *Clim. Dyn.*,  
880 27(7–8), 787–813, doi:10.1007/s00382-006-0158-0, 2006.
- 881 Hov, Ø., Hjøllø, B. A. and Eliassen, A.: Transport distance of ammonia and  
882 ammonium in Northern Europe: 2. Its relation to emissions of SO<sub>2</sub> and NO<sub>x</sub>, *J.*  
883 *Geophys. Res.*, 99(D9), 18749, doi:10.1029/94jd00910, 1994.
- 884 Kajino, M., Ueda, H., Satsumabayashi, H. and An, J.: Impacts of the eruption of  
885 Miyakejima Volcano on air quality over far east Asia, *J. Geophys. Res. D Atmos.*,  
886 109(21), 1–11, doi:10.1029/2004JD004762, 2004.
- 887 Kean, A. J., Littlejohn, D., Ban-Weiss, G. A., Harley, R. A., Kirchstetter, T. W. and  
888 Lunden, M. M.: Trends in on-road vehicle emissions of ammonia, *Atmos. Environ.*,  
889 43(8), 1565–1570, doi:10.1016/j.atmosenv.2008.09.085, 2009.
- 890 Kharol, S. K., Shephard, M. W., McLinden, C. A., Zhang, L., Sioris, C. E., O'Brien, J.  
891 M., Vet, R., Cady-Pereira, K. E., Hare, E., Siemons, J. and Krotkov, N. A.: Dry  
892 Deposition of Reactive Nitrogen From Satellite Observations of Ammonia and  
893 Nitrogen Dioxide Over North America, *Geophys. Res. Lett.*, 45(2), 1157–1166,  
894 doi:10.1002/2017GL075832, 2018.
- 895 Klimont, Z., Kupiainen, K., Heyes, C., Purohit, P., Cofala, J., Rafaj, P., Borcken-  
896 Kleefeld, J. and Schöpp, W.: Global anthropogenic emissions of particulate matter  
897 including black carbon, *Atmos. Chem. Phys.*, 17, 8681–8723, doi:10.5194/acp-17- 50  
898 8681-2017, 2017.
- 899 Krinner, G., Viovy, N., de Noblet-Ducoudré, N., Ogée, J., Polcher, J., Friedlingstein,  
900 P., Ciais, P., Sitch, S. and Prentice, I. C.: A dynamic global vegetation model for  
901 studies of the coupled atmosphere-biosphere system, *Global Biogeochem. Cycles*,  
902 19(1), n/a–n/a, doi:10.1029/2003GB002199, 2005.
- 903 Kuttippurath, J., Singh, A., Dash, S. P., Mallick, N., Clerbaux, C., Van Damme, M.,  
904 Clarisse, L., Coheur, P. F., Raj, S., Abhishek, K. and Varikoden, H.: Record high  
905 levels of atmospheric ammonia over India: Spatial and temporal analyses, *Sci. Total*  
906 *Environ.*, 740, 139986, doi:10.1016/j.scitotenv.2020.139986, 2020.
- 907 Lachatre, M., Fortems-Cheiney, A., Foret, G., Siour, G., Dufour, G., Clarisse, L.,  
908 Clerbaux, C., Coheur, P. F., Van Damme, M. and Beekmann, M.: The unintended  
909 consequence of SO<sub>2</sub> and NO<sub>2</sub> regulations over China: Increase of ammonia levels  
910 and impact on PM<sub>2.5</sub> concentrations, *Atmos. Chem. Phys.*, 19(10), 6701–6716,  
911 doi:10.5194/acp-19-6701-2019, 2019.
- 912 Leip, A., Billen, G., Garnier, J., Grizzetti, B., Lassaletta, L., Reis, S., Simpson, D.,  
913 Sutton, M. a, de Vries, W., Weiss, F. and Westhoek, H.: Impacts of European  
914 livestock production: nitrogen, sulphur, phosphorus and greenhouse gas emissions,  
915 land-use, water eutrophication and biodiversity, *Environ. Res. Lett.*, 10(11), 115004,  
916 doi:10.1088/1748-9326/10/11/115004, 2015.
- 917 Lelieveld, J., Evans, J. S., Fnais, M., Giannadaki, D. and Pozzer, A.: The contribution  
918 of outdoor air pollution sources to premature mortality on a global scale., *Nature*,  
919 525(7569), 367–71, doi:10.1038/nature15371, 2015.
- 920 Li, C., Martin, R. V., Shephard, M. W., Pereira, K. C., Cooper, M. J., Kaiser, J., Lee,  
921 C. J., Zhang, L. and Henze, D. K.: Assessing the Iterative Finite Difference Mass  
922 Balance and 4D - Var Methods to Derive Ammonia Emissions Over North America  
923 Using Synthetic Observations, , 4222–4236, doi:10.1029/2018JD030183, 2019.
- 924 Lin, J. T., McElroy, M. B. and Boersma, K. F.: Constraint of anthropogenic NO<sub>x</sub>  
925 emissions in China from different sectors: A new methodology using multiple satellite  
926 retrievals, *Atmos. Chem. Phys.*, 10(1), 63–78, doi:10.5194/acp-10-63-2010, 2010.



- 927 Liu, L., Zhang, X., Wong, A. Y. H., Xu, W., Liu, X., Li, Y., Mi, H., Lu, X., Zhao, L.,  
928 Wang, Z. and Wu, X.: Estimating global surface ammonia concentrations inferred  
929 from satellite retrievals, *Atmos. Chem. Phys.*, (19), 12051–12066, doi:10.5194/acp-  
930 19-12051-2019, 2019.
- 931 Liu, M., Huang, X., Song, Y., Xu, T., Wang, S., Wu, Z., Hu, M., Zhang, L., Zhang, Q.,  
932 Pan, Y. and Zhu, T.: Rapid SO<sub>2</sub> emission reductions significantly increase  
933 tropospheric ammonia concentrations over the North China Plain, *Atmos. Chem.*  
934 *Phys.*, (18), 17933–17943, doi:10.5194/acp-18-17933-2018, 2018.
- 935 Makar, P. A., Moran, M. D., Zheng, Q., Cousineau, S., Sassi, M., Duhamel, A.,  
936 Besner, M., Davignon, D., Crevier, L. P. and Bouchet, V. S.: Modelling the impacts of  
937 ammonia emissions reductions on North American air quality, *Atmos. Chem. Phys.*,  
938 9(18), 7183–7212, doi:10.5194/acp-9-7183-2009, 2009.
- 939 Malm, W. C.: Spatial and monthly trends in speciated fine particle concentration in  
940 the United States, *J. Geophys. Res.*, 109(D3), D03306, doi:10.1029/2003JD003739,  
941 2004.
- 942 Malm, W. C., Schichtel, B. A., Barna, M. G., Gebhart, K. A., Rodriguez, M. A., Collett,  
943 J. L., Carrico, C. M., Benedict, K. B., Prenni, A. J. and Kreidenweis, S. M.: Aerosol  
944 species concentrations and source apportionment of ammonia at Rocky Mountain  
945 National Park, *J. Air Waste Manag. Assoc.*, 63(11), 1245–1263,  
946 doi:10.1080/10962247.2013.804466, 2013.
- 947 van Marle, M. J. E., Field, R. D., van der Werf, G. R., Estrada de Wagt, I. A.,  
948 Houghton, R. A., Rizzo, L. V., Artaxo, P. and Tsigaridis, K.: Fire and deforestation  
949 dynamics in Amazonia (1973–2014), *Global Biogeochem. Cycles*, 31(1), 24–38,  
950 doi:10.1002/2016GB005445, 2017.
- 951 McQuilling, A. M.: Ammonia emissions from livestock in the United States: From farm  
952 emissions models to a new national inventory, ProQuest Diss. Theses, 168 [online]  
953 Available from:  
954 [https://search.proquest.com/docview/1841254436?accountid=133571%0Ahttp://www](https://search.proquest.com/docview/1841254436?accountid=133571%0Ahttp://www.yidu.edu.cn/educhina/educhina.do?artifact=&svalue=Ammonia+emissions+from+live+stock+in+the+United+States%3A+From+farm+emissions+models+to+a+new+nation+al+inventory&styp=2&s=on%0Ah)  
955 [.yidu.edu.cn/educhina/educhina.do?artifact=&svalue=Ammonia+emissions+from+live](https://search.proquest.com/docview/1841254436?accountid=133571%0Ahttp://www.yidu.edu.cn/educhina/educhina.do?artifact=&svalue=Ammonia+emissions+from+live+stock+in+the+United+States%3A+From+farm+emissions+models+to+a+new+nation+al+inventory&styp=2&s=on%0Ah)  
956 [stock+in+the+United+States%3A+From+farm+emissions+models+to+a+new+nation](https://search.proquest.com/docview/1841254436?accountid=133571%0Ahttp://www.yidu.edu.cn/educhina/educhina.do?artifact=&svalue=Ammonia+emissions+from+live+stock+in+the+United+States%3A+From+farm+emissions+models+to+a+new+nation+al+inventory&styp=2&s=on%0Ah)  
957 [al+inventory&styp=2&s=on%0Ah](https://search.proquest.com/docview/1841254436?accountid=133571%0Ahttp://www.yidu.edu.cn/educhina/educhina.do?artifact=&svalue=Ammonia+emissions+from+live+stock+in+the+United+States%3A+From+farm+emissions+models+to+a+new+nation+al+inventory&styp=2&s=on%0Ah), 2016.
- 958 Min Hao, W., Petkov, A., Nordgren, B. L., Corley, R. E., Silverstein, R. P., Urbanski,  
959 S. P., Evangeliou, N., Balkanski, Y. and Kinder, B. L.: Daily black carbon emissions  
960 from fires in northern Eurasia for 2002–2015, *Geosci. Model Dev.*, 9(12),  
961 doi:10.5194/gmd-9-4461-2016, 2016.
- 962 Möller, D. and Schieferdecker, H.: A relationship between agricultural NH<sub>3</sub>  
963 emissions and the atmospheric SO<sub>2</sub> content over industrial areas, *Atmos. Environ.*,  
964 19(5), 695–700, doi:10.1016/0004-6981(85)90056-3, 1985.
- 965 Norman, M. and Leck, C.: Distribution of marine boundary layer ammonia over the  
966 Atlantic and Indian Oceans during the Aerosols99 cruise, *J. Geophys. Res. D*  
967 *Atmos.*, 110(16), 1–11, doi:10.1029/2005JD005866, 2005.
- 968 Pan, Y., Tian, S., Zhao, Y., Zhang, L., Zhu, X., Gao, J., Huang, W., Zhou, Y., Song,  
969 Y., Zhang, Q. and Wang, Y.: Identifying Ammonia Hotspots in China Using a National  
970 Observation Network, *Environ. Sci. Technol.*, 52(7), 3926–3934,  
971 doi:10.1021/acs.est.7b05235, 2018.
- 972 Parzen, E.: On the Estimation of Probability Density Functions and Mode, *Ann. Math.*  
973 *Stat.*, 33, 1065–1076, 1962.
- 974 Paulot, F., Jacob, D. J., Pinder, R. W., Bash, J. O., Travis, K. and Henze, D. K.:  
975 Ammonia emissions in the United States, European Union, and China derived by  
976 high-resolution inversion of ammonium wet deposition data: Interpretation with a new



- 977 agricultural emissions inventory (MASAGE-NH<sub>3</sub>), *J. Geophys. Res. Atmos.*, 119(7),  
978 4343–4364, doi:10.1002/2013JD021130, 2014.
- 979 Pinder, R. W., Gilliland, A. B. and Dennis, R. L.: Environmental impact of  
980 atmospheric NH<sub>3</sub> emissions under present and future conditions in the  
981 eastern United States, *Geophys. Res. Lett.*, 35(12), 1–6,  
982 doi:10.1029/2008GL033732, 2008.
- 983 Pope III, C. A., Burnett, R. T., Thun, M. J., Calle, E. E., Krewski, D. and Thurston, G.  
984 D.: Lung Cancer, Cardiopulmonary Mortality, and Long-term Exposure to Fine  
985 Particulate Air Pollution, *J. Am. Med. Assoc.*, 287(9), 1132–1141,  
986 doi:10.1001/jama.287.9.1132, 2002.
- 987 Quinn, P. K., Bates, T. S. and Johnson, J. E.: Interactions Between the Sulfur and  
988 Reduced Nitrogen Cycles Over the Central Pacific Ocean, *J. Geophys. Res.*,  
989 95(D10), 16405–16416, 1990.
- 990 R'Honi, Y., Clarisse, L., Clerbaux, C., Hurtmans, D., Duflot, V., Turquety, S., Ngadi,  
991 Y. and Coheur, P. F.: Exceptional emissions of NH<sub>3</sub> and HCOOH in the 2010  
992 Russian wildfires, *Atmos. Chem. Phys.*, 13(1), 4171–4181, doi:10.5194/acp-13-4171-  
993 2013, 2013.
- 994 Reche, C., Viana, M., Pandolfi, M., Alastuey, A., Moreno, T., Amato, F., Ripoll, A. and  
995 Querol, X.: Urban NH<sub>3</sub> levels and sources in a Mediterranean environment, *Atmos.*  
996 *Environ.*, 57, 153–164, doi:10.1016/j.atmosenv.2012.04.021, 2012.
- 997 Reis, S., Pinder, R. W., Zhang, M., Lijie, G. and Sutton, M. A.: Reactive nitrogen in  
998 atmospheric emission inventories, *Atmos. Chem. Phys.*, 9(19), 7657–7677,  
999 doi:10.5194/acp-9-7657-2009, 2009.
- 1000 Renka, R. J.: Multivariate Interpolation of Large Sets of Scattered Data, *ACM Trans.*  
1001 *Math. Softw.*, 14(2), 139–148, doi:10.1145/45054.45055, 1988.
- 1002 Schulz, M.: Constraining model estimates of the aerosol Radiative Forcing,  
1003 Université Pierre et Marie Curie, Paris VI., 2007.
- 1004 Scott, D. W.: Multivariate density estimation: Theory, practice, and visualization:  
1005 Second edition., 2015.
- 1006 Seinfeld, J. H. and Pandis, S. N.: Atmospheric Chemistry and Physics. From Air  
1007 Pollution to Climate Change, 2nd ed., John Wiley & Sons, NY., 2000.
- 1008 Shephard, M. W. and Cady-Pereira, K. E.: Cross-track Infrared Sounder (CrIS)  
1009 satellite observations of tropospheric ammonia, *Atmos. Meas. Tech.*, 8(3), 1323–  
1010 1336, doi:10.5194/amt-8-1323-2015, 2015.
- 1011 Shephard, M. W., McLinden, C. A., Cady-Pereira, K. E., Luo, M., Moussa, S. G.,  
1012 Leithead, A., Liggio, J., Staebler, R. M., Akingunola, A., Makar, P., Lehr, P., Zhang,  
1013 J., Henze, D. K., Millet, D. B., Bash, J. O., Zhu, L., Wells, K. C., Capps, S. L.,  
1014 Chaliyakunnel, S., Gordon, M., Hayden, K., Brook, J. R., Wolde, M. and Li, S. M.:  
1015 Tropospheric Emission Spectrometer (TES) satellite observations of ammonia,  
1016 methanol, formic acid, and carbon monoxide over the Canadian oil sands: Validation  
1017 and model evaluation, *Atmos. Meas. Tech.*, 8(12), 5189–5211, doi:10.5194/amt-8-  
1018 5189-2015, 2015.
- 1019 Shephard, M. W., Dammers, E., Cady-Pereira, K., Kharol, S., Thompson, J.,  
1020 Gainariu-Matz, Y., Zhang, J., A. McLinden, C., Kovachik, A., Moran, M., Bittman, S.,  
1021 E. Sioris, C., Griffin, D., J. Alvarado, M., Lonsdale, C., Savic-Jovcic, V. and Zheng,  
1022 Q.: Ammonia measurements from space with the Cross-track Infrared Sounder:  
1023 Characteristics and applications, *Atmos. Chem. Phys.*, 20(4), 2277–2302,  
1024 doi:10.5194/acp-20-2277-2020, 2020.
- 1025 Someya, Y., Imasu, R., Shiomi, K. and Saitoh, N.: Atmospheric ammonia retrieval  
1026 from the TANSO-FTS / GOSAT thermal infrared sounder, , 1990, 309–321, 2020.



- 1027 Sørensen, L. L., Hertel, O., Skjøth, C. A., Lund, M. and Pedersen, B.: Fluxes of  
1028 ammonia in the coastal marine boundary layer, *Atmos. Environ.*, 37(SUPPL. 1), 167–  
1029 177, doi:10.1016/S1352-2310(03)00247-4, 2003.
- 1030 Stevens, C. J., Dupr, C., Dorland, E., Gaudnik, C., Gowing, D. J. G., Bleeker, A.,  
1031 Diekmann, M., Alard, D., Bobbink, R., Fowler, D., Corcket, E., Mountford, J. O.,  
1032 Vandvik, V., Aarrestad, P. A., Muller, S. and Dise, N. B.: Nitrogen deposition  
1033 threatens species richness of grasslands across Europe, *Environ. Pollut.*, 158(9),  
1034 2940–2945, doi:10.1016/j.envpol.2010.06.006, 2010.
- 1035 Streets, D. G., Canty, T., Carmichael, G. R., de Foy, B., Dickerson, R. R., Duncan, B.  
1036 N., Edwards, D. P., Haynes, J. A., Henze, D. K., Houyoux, M. R., Jacob, D. J.,  
1037 Krotkov, N. A., Lamsal, L. N., Liu, Y., Lu, Z., Martin, R. V., Pfister, G. G., Pinder, R.  
1038 W., Salawitch, R. J. and Wecht, K. J.: Emissions estimation from satellite retrievals: A  
1039 review of current capability, *Atmos. Environ.*, 77, 1011–1042,  
1040 doi:https://doi.org/10.1016/j.atmosenv.2013.05.051, 2013.
- 1041 Sutton, M. A., Fowler, D., Moncrieff, J. B. and Storeton-West, R. L.: The exchange of  
1042 atmospheric ammonia with vegetated surfaces. II: Fertilized vegetation, *Q. J. R.  
1043 Meteorol. Soc.*, 119(513), 1047–1070, doi:10.1002/qj.49711951310, 1993.
- 1044 Sutton, M. A., Dragosits, U., Tang, Y. S. and Fowler, D.: Ammonia emissions from  
1045 non-agricultural sources in the UK, , 34(August 1999), 2000.
- 1046 Sutton, M. A., Erisman, J. W., Dentener, F. and Möller, D.: Ammonia in the  
1047 environment: From ancient times to the present, *Environ. Pollut.*, 156(3), 583–604,  
1048 doi:10.1016/j.envpol.2008.03.013, 2008.
- 1049 Tanvir, A., Khokhar, M. F., Javed, Z., Sandhu, O., Mustansar, T. and Shoaib, A.:  
1050 Spatiotemporal evolution of atmospheric ammonia columns over the indo-gangetic  
1051 plain by exploiting satellite observations, *Adv. Meteorol.*, 2019,  
1052 doi:10.1155/2019/7525479, 2019.
- 1053 Turner, A. J., Henze, D. K., Martin, R. V. and Hakami, A.: The spatial extent of  
1054 source influences on modeled column concentrations of short-lived species,  
1055 *Geophys. Res. Lett.*, 39(12), 1–5, doi:10.1029/2012GL051832, 2012.
- 1056 Uematsu, M., Toratani, M., Kajino, M., Narita, Y., Senga, Y. and Kimoto, T.:  
1057 Enhancement of primary productivity in the western North Pacific caused by the  
1058 eruption of the Miyake-jima Volcano, *Geophys. Res. Lett.*, 31(6), n/a-n/a,  
1059 doi:10.1029/2003gl018790, 2004.
- 1060 Vincenty, T.: Direct and inverse solutions of geodesics on the ellipsoid with  
1061 application of nested equations, *Surv. Rev.* XXIII (misprinted as XXII), 176, 88–93,  
1062 1975.
- 1063 De Vries, W., Kros, J., Reinds, G. J. and Butterbach-Bahl, K.: Quantifying impacts of  
1064 nitrogen use in European agriculture on global warming potential, *Curr. Opin.  
1065 Environ. Sustain.*, 3(5), 291–302, doi:10.1016/j.cosust.2011.08.009, 2011.
- 1066 Warner, J. X., Dickerson, R. R., Wei, Z., Strow, L. L., Wang, Y. and Liang, Q.:  
1067 Increased atmospheric ammonia over the world's major agricultural areas detected  
1068 from space, *Geophys. Res. Lett.*, 1–10, doi:10.1002/2016GL072305, 2017.
- 1069 Webb, J., Menzi, H., Pain, B. F., Misselbrook, T. H., Dämmgen, U., Hendriks, H. and  
1070 Döhler, H.: Managing ammonia emissions from livestock production in Europe,  
1071 *Environ. Pollut.*, 135(3 SPEC. ISS.), 399–406, doi:10.1016/j.envpol.2004.11.013,  
1072 2005.
- 1073 Whitburn, S., Van Damme, M., Kaiser, J. W., Van Der Werf, G. R., Turquety, S.,  
1074 Hurtmans, D., Clarisse, L., Clerbaux, C. and Coheur, P. F.: Ammonia emissions in  
1075 tropical biomass burning regions: Comparison between satellite-derived emissions  
1076 and bottom-up fire inventories, *Atmos. Environ.*, 121, 42–54,

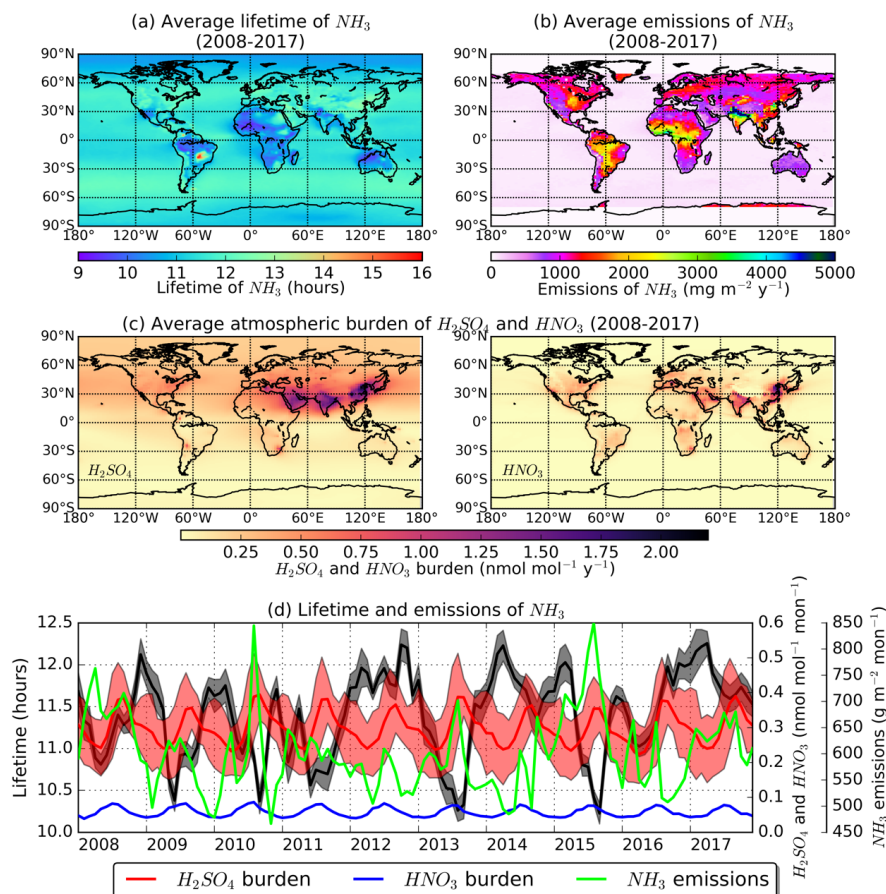


1077 doi:10.1016/j.atmosenv.2015.03.015, 2014.  
1078 Whitburn, S., Van Damme, M., Clarisse, L., Bauduin, S., Heald, C. L., Hadji-Lazaro,  
1079 J., Hurtmans, D., Zondlo, M. A., Clerbaux, C. and Coheur, P. F.: A flexible and robust  
1080 neural network IASI-NH<sub>3</sub> retrieval algorithm, *J. Geophys. Res.*, 121(11), 6581–6599,  
1081 doi:10.1002/2016JD024828, 2016a.  
1082 Whitburn, S., Damme, M. Van, Clarisse, L., Turquety, S., Clerbaux, C. and Coheur,  
1083 P. -: Peat fires doubled annual ammonia emissions in Indonesia during the 2015 El  
1084 Niño, *Geophys. Res. Lett.*, doi:10.1002/2016GL070620, 2016b.  
1085 Xu, L. and Penner, J. E.: Global simulations of nitrate and ammonium aerosols and  
1086 their radiative effects, *Atmos. Chem. Phys.*, 12(20), 9479–9504, doi:10.5194/acp-12-  
1087 9479-2012, 2012.  
1088 Xu, P., Liao, Y. J., Lin, Y. H., Zhao, C. X., Yan, C. H., Cao, M. N., Wang, G. S. and  
1089 Luan, S. J.: High-resolution inventory of ammonia emissions from agricultural  
1090 fertilizer in China from 1978 to 2008, *Atmos. Chem. Phys.*, 16(3), 1207–1218,  
1091 doi:10.5194/acp-16-1207-2016, 2016.  
1092 Xu, R. T., Pan, S. F., Chen, J., Chen, G. S., Yang, J., Dangal, S. R. S., Shepard, J.  
1093 P. and Tian, H. Q.: Half-Century Ammonia Emissions From Agricultural Systems in  
1094 Southern Asia: Magnitude, Spatiotemporal Patterns, and Implications for Human  
1095 Health, *GeoHealth*, 2(1), 40–53, doi:10.1002/2017gh000098, 2018.  
1096 Yang, K., Krotkov, N. A., Krueger, A. J., Carn, S. A., Bhartia, P. K. and Levelt, P. F.:  
1097 Retrieval of large volcanic SO<sub>2</sub> columns from the Aura Ozone Monitoring  
1098 Instrument: Comparison and limitations, *J. Geophys. Res. Atmos.*, 112(24), 1–14,  
1099 doi:10.1029/2007JD008825, 2007.  
1100 Zavyalov, V., Esplin, M., Scott, D., Esplin, B., Bingham, G., Hoffman, E., Lietzke, C.,  
1101 Predina, J., Frain, R., Suwinski, L., Han, Y., Major, C., Graham, B. and Phillips, L.:  
1102 Noise performance of the CrIS instrument, , 118, 108–120,  
1103 doi:10.1002/2013JD020457, 2013.  
1104 Zhao, C. and Wang, Y.: Assimilated inversion of NO<sub>x</sub> emissions over east Asia using  
1105 OMINO<sub>2</sub> column measurements, *Geophys. Res. Lett.*, 36(6), 1–5,  
1106 doi:10.1029/2008GL037123, 2009.  
1107 Zhu, L., Henze, D. K., Cady-Pereira, K. E., Shephard, M. W., Luo, M., Pinder, R. W.,  
1108 Bash, J. O. and Jeong, G. R.: Constraining U.S. ammonia emissions using TES  
1109 remote sensing observations and the GEOS-Chem adjoint model, *J. Geophys. Res.*  
1110 *Atmos.*, 118(8), 3355–3368, doi:10.1002/jgrd.50166, 2013.  
1111 Zhu, L., Henze, D. K., Bash, J. O., Cady-Pereira, K. E., Shephard, M. W., Luo, M.  
1112 and Capps, S. L.: Sources and Impacts of Atmospheric NH<sub>3</sub>: Current Understanding  
1113 and Frontiers for Modeling, Measurements, and Remote Sensing in North America,  
1114 *Curr. Pollut. Reports*, 1(2), 95–116, doi:10.1007/s40726-015-0010-4, 2015.  
1115  
1116



1117 **FIGURE LEGENDS**

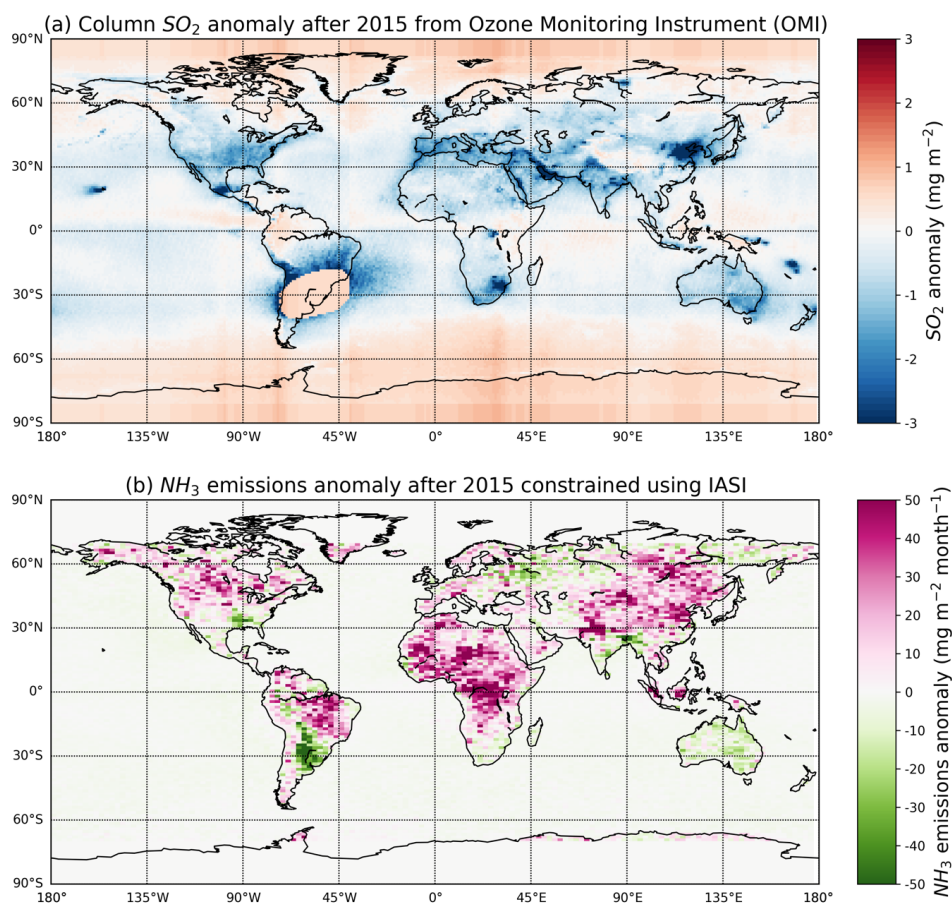
1118



1119

1120 Figure 1. (a) Average model lifetime of ammonia calculated from the LMDz-OR-INCA model,  
1121 (b) total annual emissions averaged over the 10-year period, (c) atmospheric burden of the  
1122 reactants sulfuric and nitric acid calculated in the model, and (d) monthly timeseries of lifetime  
1123 (black), ammonia emissions (green), sulfate (red) and nitrate column concentrations (blue) for  
1124 the whole 10-year period.

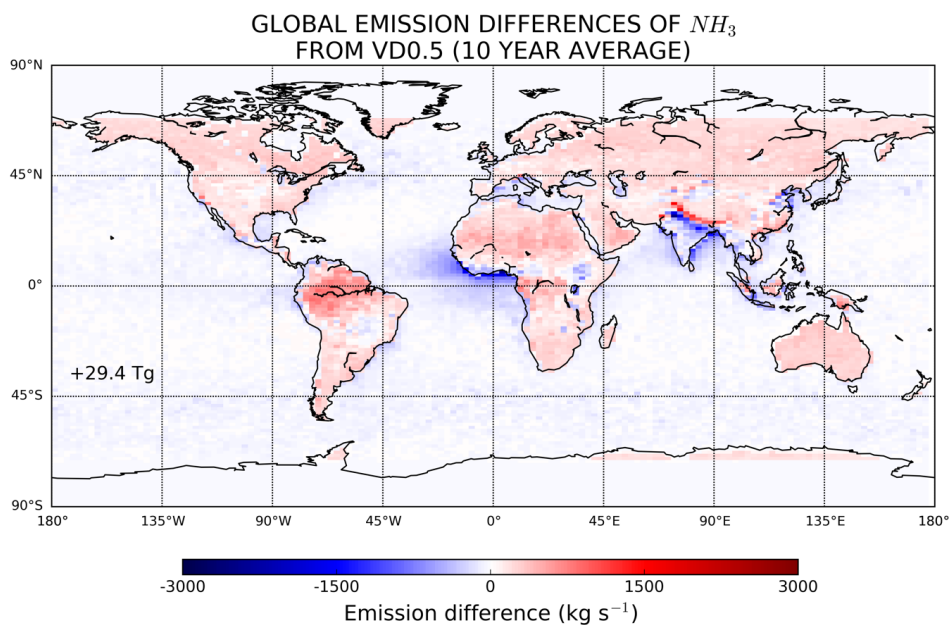
1125



1126

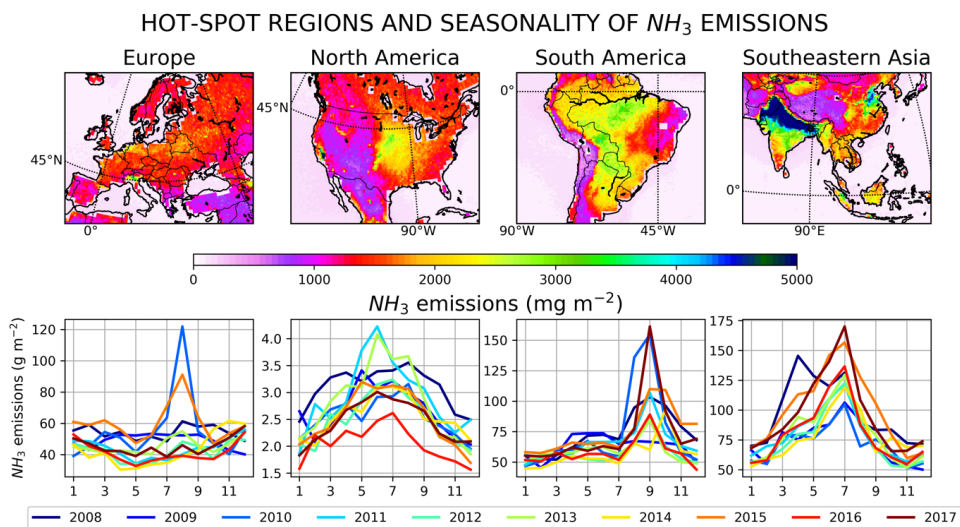
1127 Figure 2. (a) Annual average total column sulfur dioxide anomaly after 2015 from OMI, and  
1128 (b) annual average emission anomaly of ammonia calculated from IASI in the present study  
1129 (NE).

1130



1131  
1132 Figure 3. Global differences of ammonia emissions calculated in the present study (NE) from  
1133 those calculated using Van Damme et al. (2018) gridded concentrations applying a constant  
1134 lifetime of 0.5 days (VD0.5). The results are given as 10-year average (2008–2017) and the  
1135 number denotes the annual difference in the emissions.

1136



1137

1138

Figure 4. Total annual emissions of ammonia averaged over the 10-year period (2008–2017) in Europe, North and South America and Southeastern Asia, which are regions characterized by the largest contribution to global ammonia budget. In the bottom panels the monthly variation of the emissions is shown for each year of the study period.

1139

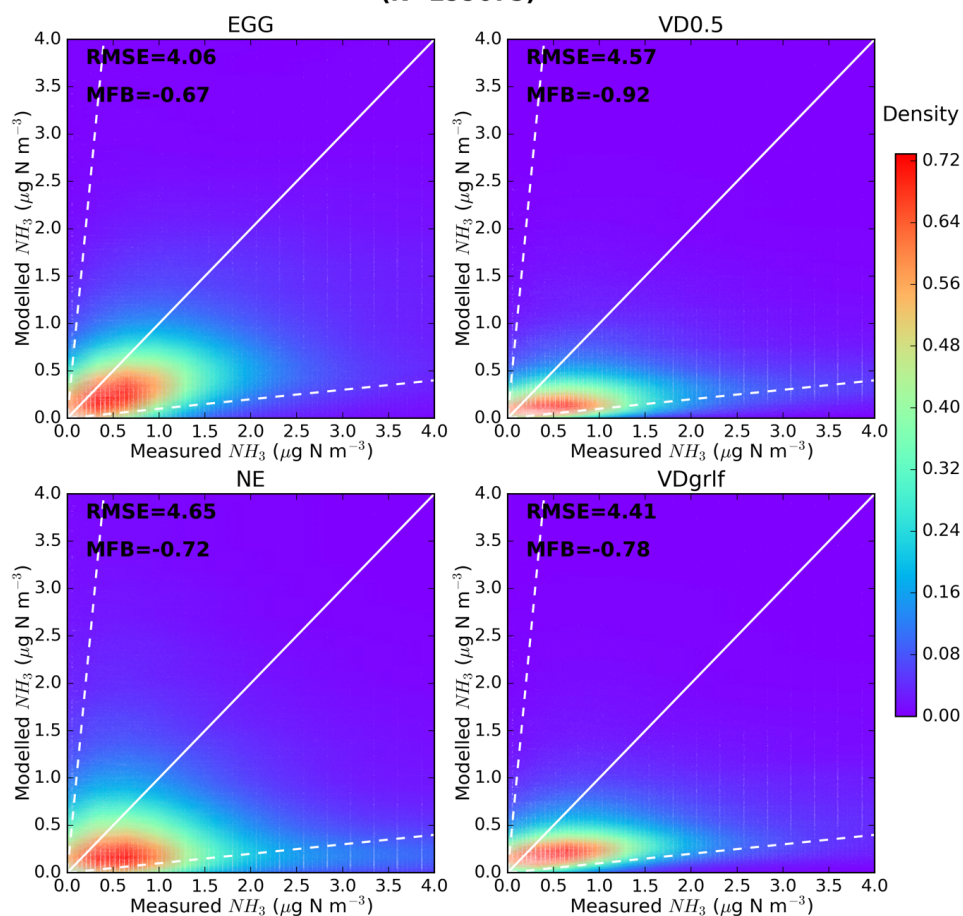
1140

1141

1142



### COMPARISON WITH OBSERVATIONS FROM EMEP (N=299075)



1143

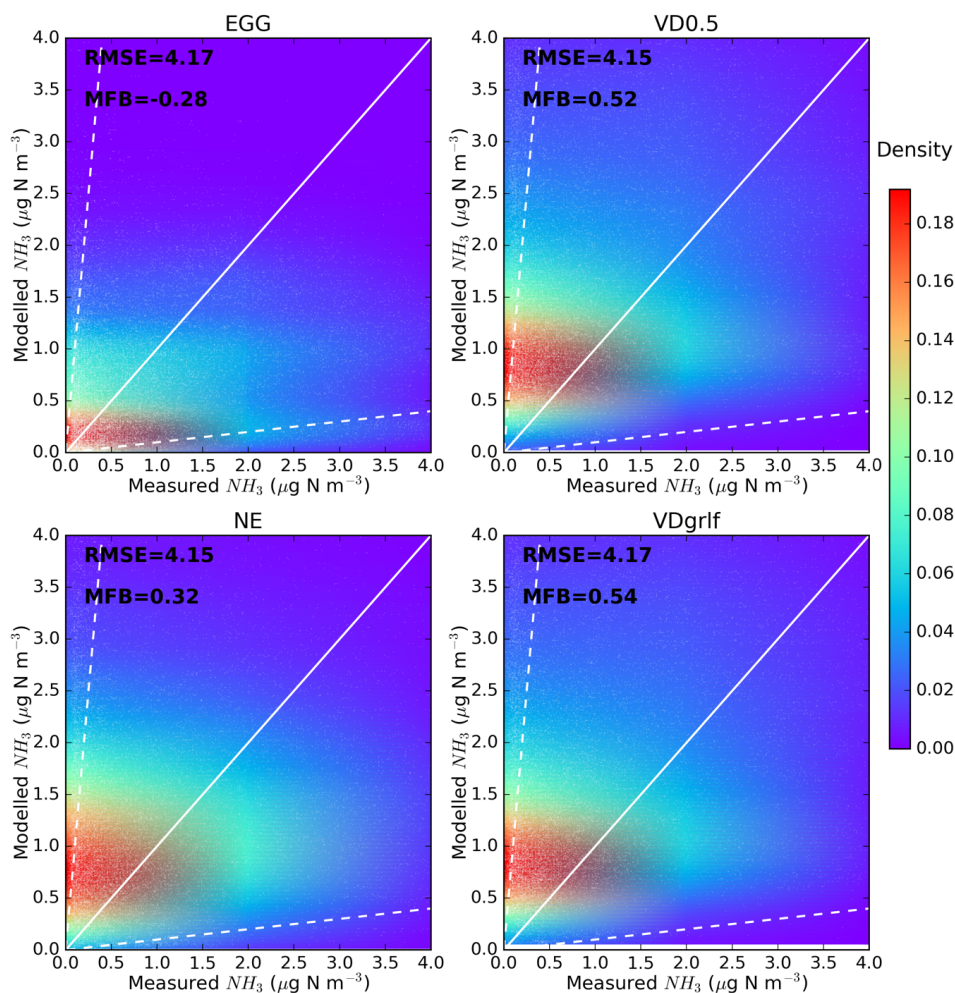
1144

Figure 5. Validation of modelled concentrations of ammonia for different emissions datasets (EGG, VD0.5, NE and VDgrlf) against ground-based measurements from EMEP for the 10-year (2008–2017) study period. Scatterplots of modelled against measured concentrations for the aforementioned emission inventories were plotted with the Kernel density estimation, which is a way to estimate the probability density function (PDF) of a random variable in a non-parametric way.

1150



### COMPARISON WITH OBSERVATIONS FROM AMON (N=27096)



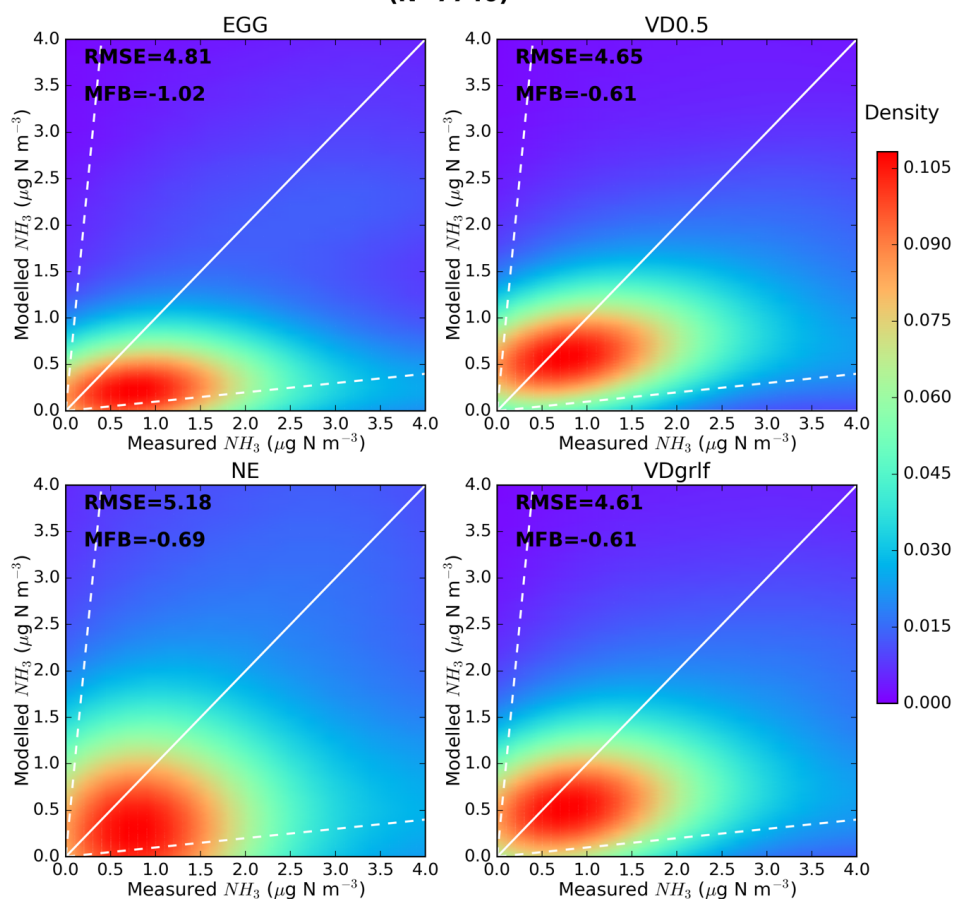
1151

1152 Figure 6. Validation of modelled concentrations of ammonia for different emissions datasets  
1153 (EGG, VD0.5, NE and VDgrlf) against ground-based measurements from AMON for the 10-  
1154 year (2008–2017) study period. Scatterplots of modelled against measured concentrations for  
1155 the aforementioned emission inventories were plotted with the Kernel density estimation, which  
1156 is a way to estimate the probability density function (PDF) of a random variable in a non-  
1157 parametric way.

1158



### COMPARISON WITH OBSERVATIONS FROM EANET (N=7740)



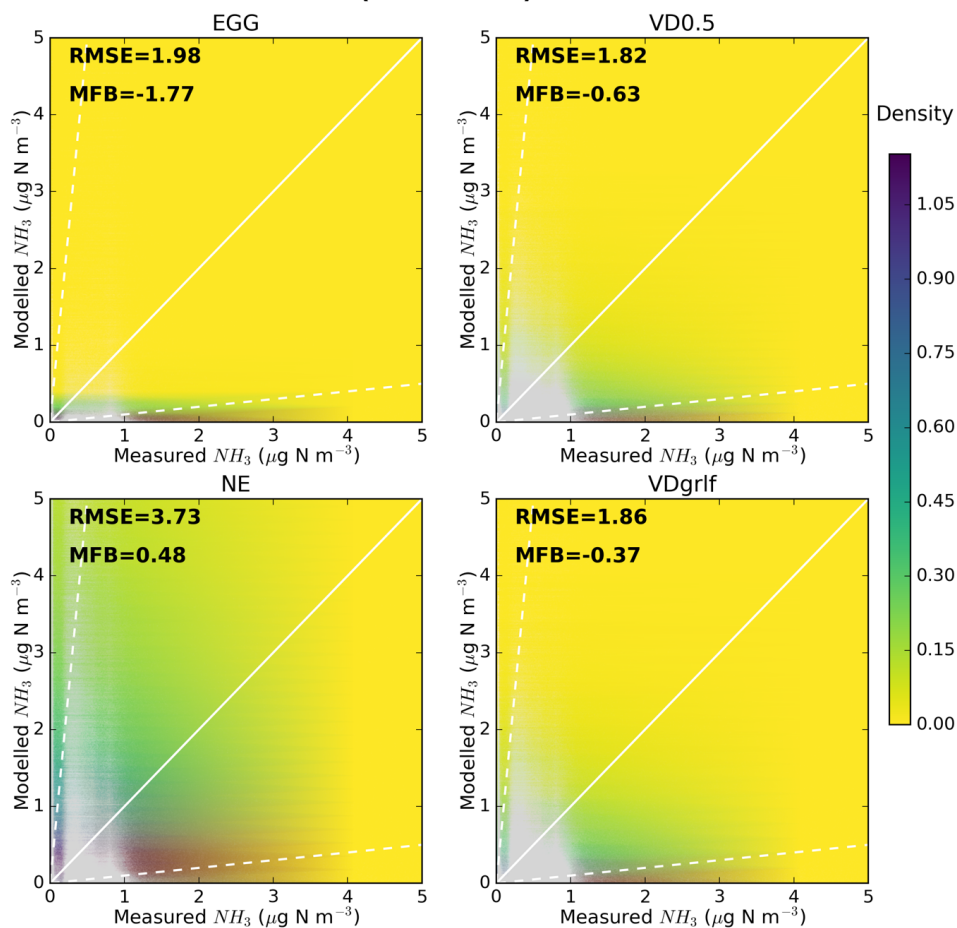
1159

1160 Figure 7. Validation of modelled concentrations of ammonia for different emissions datasets  
1161 (EGG, VD0.5, NE and VDgrlf) against ground-based measurements from EANET for the 10-  
1162 year (2008–2017) study period. Scatterplots of modelled against measured concentrations for  
1163 the aforementioned emission inventories were plotted with the Kernel density estimation, which  
1164 is a way to estimate the probability density function (PDF) of a random variable in a non-  
1165 parametric way.

1166



**COMPARISON WITH OBSERVATIONS FROM CRIS  
(N=4465037)**



1167

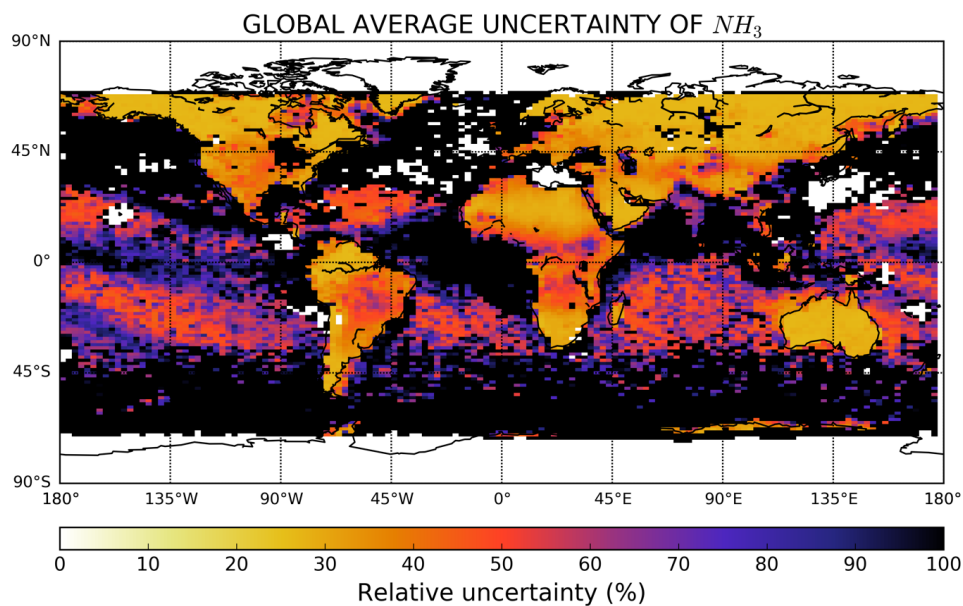
1168

Figure 8. Kernel density estimation (KDE) of the probability density function (PDF) of modelled versus CrIS concentrations of ammonia in a non-parametric way. Modelled concentrations are results of simulations using different emissions datasets (EGG, VD0.5, NE and VDgrlf) for 2012–2017.

1170

1171

1172



1173  
1174 Figure 9. 10-year average relative uncertainty of modelled surface concentrations expressed as  
1175 the standard deviation of surface concentrations from a model ensemble (Table 1) divided by  
1176 the average.  
1177



1178 Table 1. Model ensemble simulations using different emissions for ammonia that were used in  
1179 the calculations of uncertainty. Uncertainties were calculated as the standard deviation of the  
1180 surface concentrations of ammonia from the 10 ensemble members for the 10-year period  
1181 (2008–2017).

	Parameter perturbed	10-year average emissions (Tg yr <sup>-1</sup> )
Ensemble 1	$d_k = 0$ in Eq. 2	121±50.6
Ensemble 2	$d_k = 10$ in Eq. 2	175±33.3
Ensemble 3	$d_k = 20$ in Eq. 2	189±28.7
Ensemble 4	$d_k = 60$ in Eq. 2	218±15.5
Ensemble 5	$d_k = 100$ in Eq. 2	208±51.8
Ensemble 6	$d_k = 500$ in Eq. 2	223±26.5
Ensemble 7	EGG	65±2.8
Ensemble 8	VD0.5	189
Ensemble 9	NE	213±18.1
Ensemble 10	VDgrlf	201±10.4

1182

1183